Realia et naturalia

DISSERTATIONES
PHYSICAE
UNIVERSITATIS
TARTUENSIS
97

MIHKEL RÄHN

Experimental nanophotonics: single-photon sources- and nanofiber-related studies

TARTU ÜLIKOOL · UNIVERSITAS TARTUENSIS
1632

DISSERTATIONES PHYSICAE UNIVERSITATIS TARTUENSIS

97

DISSERTATIONES PHYSICAE UNIVERSITATIS TARTUENSIS
97

MIHKEL RÄHN

Experimental nanophotonics: single-photon sources- and nanofiber-related studies

UNIVERSITY OF TARTU
PRESS

This study was carried out at the Institute of Physics, University of Tartu.

The dissertation was admitted on 20.02.2015 in partial fulfilment of the requirements for the degree of Doctor of Philosophy in Physics, and was allowed for defence by the Council of the Institute of Physics, University of Tartu.

Supervisors: Dr. Viktor Palm
Institute of Physics, University of Tartu, Estonia

Dr. Ilmo Sildos
Institute of Physics, University of Tartu, Estonia

Opponents: Dr. Sergey K. Sekatskii
Laboratory of the Physics of Living Matter,
Ecole polytechnique fédérale de Lausanne, Switzerland

Defence: May 14, 2015 at University of Tartu, Estonia

The research presented in this thesis is supported by the Estonian Science Foundation projects no. ETF6543, ETF6999, ETF8167 and ETF8699, national scholarship program Kristjan Jaak, which is funded and managed by Archimedes Foundation in collaboration with the Ministry of Education and Research and partially by graduate school “Functional materials and technologies” receiving funding from the European Social Fund under project 1.2.0401.09-0079 in Estonia.

European Union
European Social Fund

Investing in your future

ARCHIMEDES

HARIDUS- JA
TEADUSMINISTEERIUM

ISSN 1406-0647
ISBN 978-9949-32-787-4 (print)
ISBN 978-9949-32-788-1 (pdf)

University of Tartu Press
www.tyk.ee

CONTENTS

LIST OF PUBLICATIONS INCLUDED IN THE THESIS

I Basov, A.A.; Rähn, M.; Vlasov, I.I.; Sildos, I.; Bolshakov, A.P.; Golubev, V.G.; Ralchenko, V.G. (2009). Spatial localization of Si-vacancy photoluminescent centers in a thin CVD nanodiamond film. Physica Status Solidi A – Applications and Materials Science, 206(9), 2009–2011.

II Vlasov, I.; Shenderova, O.; Turner, S.; Lebedev, O.; Basov, A.; Sildos, I.; Rähn, M.; Shiryaev, A.; Van Tendeloo, G. (2010). Nitrogen and luminescent nitrogen-vacancy defects in detonation nanodiamond. Small, 6(5), 687–694.

III Rähn, M.; Pärs, M.; Palm, V.; Jaaniso, R.; Hizhnyakov, V. (2010). Mesoscopic Effect of Spectral Modulation for the Light Transmitted by a SNOM Tip. Optics Communications, 283(11), 2457–2460.

IV Palm, V.; Rähn, M.; Hizhnyakov, V. (2012). Modal dispersion due to photon–plasmon coupling in a SNOM tip. Optics Communications, 285, 4579–4582.

V Palm, V.; Rähn, M.; Jäme, J.; Hizhnyakov, V. (2012). Excitation of surface plasmons in Al-coated SNOM tips. Proc. SPIE 8457, Plasmonics: Metallic Nanostructures and Their Optical Properties X, 84572S; doi:10.1117/12.929719

AUTHOR'S CONTRIBUTION

I Raman and photoluminescence characterization of samples. Design and buildup of Hanbury Brown & Twiss interferometry for characterization of defect centers. Construction of a purpose-built setup with unique hard- and software.

II Raman and photoluminescence characterization of samples by using the purpose-built setup.

III Setting up optical experiments, discovering the MSM effect, analyzing the data.

IV Experimental part of the work, participation in data analysis and preparation of the manuscript.

V Supervision of an undergraduate student (Joonas Jäme) over the experimental part of the work and the data analysis.

OTHER PUBLICATIONS OF THE DISSERTANT

a. Pärs, M.; Palm, V.; Rähn, M.; Palm, N.; Kikas, J. (2008). Room-temperature single-molecule fluorescence imaging for terrylene in biphenyl single crystals. Journal of Luminescence, 128(5–6), 838–841.

b. Alles, H.; Aarik, J.; Aidla, A.; Fay, A.; Kozlova, J.; Niilisk, A.; Pärs, M.; Rähn, M.; Wiesner, M.; Hakonen, P.; Sammelselg, V. (2011). Atomic layer deposition of HfO2 on graphene from HfCl4 and H2O. Central European Journal of Physics, 9(2), 319–324.

1. INTRODUCTION

1.1. Basics of single-molecule spectroscopy

Single-quantum-system optical solid-state emitters (e.g. single impurity molecules, defects, quantum dots) have lately been among the hot research topics due to their possible applications as optical nanoprobes or single-photon emitters [1–8]. Due to historical reasons, we will further refer to the correspondent research field as single-molecule spectroscopy (SMS). For such quantum-optical applications as quantum cryptography or quantum computing, generation of single photons on demand is of great importance [9].

Yet, in conventional spectroscopy experiments (measurements of absorption, luminescence, scattering) one is dealing with huge amounts of single molecules (emitters), and an averaged optical information is obtained. Upon excitation, every single emitter of the ensemble spontaneously emits a photon independently in time. Thus in the case of photoluminescence we have an uncorrelated photon flux.

One of the possibilities to reduce the number of emitters is to introduce a spatial selectivity by using a microscope to excite a small area of the sample and to collect the signal from a microvolume. By applying a confocal microscope one can have both the depth- and the lateral selection. Usually a lateral spatial resolution of ~0.5 μm and a depth resolution of ~1 μm can be easily achieved. In this way a spatial structure of the sample can be revealed on the scale of a micrometer. To ensure that only one single-emitter center is excited by a focused laser beam and selected for detection by a confocal microscope, samples with low concentration of about 10^{-10} mole/liter (which means keeping on average only one center per volume of 16.6 μm^3) have to be prepared.

A single impurity molecule can act as a nano-sensor, providing information on its nanoscale environment and thus helping to reveal the heterogeneity and dynamical processes in the host material. Ideally, a useful single emitter should have a large absorption cross-section and a high quantum yield, as well as a considerable photostability. Only few of so far examined molecules can fulfill all of these demands at the same time. But quite outstanding, especially at room temperature (RT), are the properties of several types of optical defects in diamonds [10, 11], such as nitrogen-vacancy (NV) [12], silica-vacancy (SiV) [13], nickel-nitrogen complex (NE8) [14], and xenon-vacancy (XeV) [15]. Important parameters estimated for some promising single-emitter centers are presented in Table 1.

Specific correlation phenomena as photon bunching and anti-bunching can be used to recognize a single quantum emitter [16–18]. In the case of a three-level (singlet-singlet-triplet) system the effect of bunching reflects the lifetime of a metastable (triplet) state or a “dark state”, where the system is temporally “hidden”, i.e. not available for photoexcitation on frequencies that normally can excite it from the (singlet) ground state to the (singlet) excited state. The effect of anti-bunching is related to the spontaneous lifetime of excited state τ_S: being once excited, the system cannot absorb any photons from the same frequency range while staying in the excited state (this can be considered as a kind of light-induced transparency). It is important to operate in a nearly-linear regime and avoid the saturation, which can cause a dramatic drop of the signal-to-noise ratio (SNR) at higher excitation intensities [19].

Historically, the first successful SMS experiments have been performed with pentacene impurity molecules in a low-temperature crystalline p-terphenyl matrix [20]. In the case of low-temperature SMS, very narrow zero-phonon lines enable highly-selective spectral detection or excitation by tunable and extremely narrow-line single-frequency lasers. At Institute of Physics in Tartu, a pioneering work of this type has been published by K. Rebane, V. Palm, and A. Suisalu [21].

Table 1. Some of the most promising single-emitter centers

Center	Host	Spontaneous lifetime τ_s	Huang-Rhys factor	Quantum yield	Stability (RT)	Ref.
NV	diamond	23 ns	3.21	~1	stable	[12, 22]
SiV	diamond	1–4 ns	0.24	0.05	stable	[13, 23]
NE8	diamond	11.5 ns	0.35	0.7	stable	[14, 22]
XeV	diamond	N.A.	0.69	N.A.	stable	[15]
Terrylene molecule	organic matrix	4 ns	N.A.	0.7–1	photo-chemical reaction with free oxygen	[6, 24, a]

1.2. Mesoscopic effect of spectral modulation in nanofibers

It can be shown theoretically for a broadband light propagating in a multimode optical waveguide that an interference of a small number of photonic modes with finite differences of eikonals, i.e. finite optical path differences (OPD), can result in a high-visibility spectral modulation of the output light [25, III]. No visible regular modulation is expected in the case of a large number of modes. In practice, mesoscopic (or even subwavelength) features are necessary to limit the number of transmitted modes – thus we refer to this phenomenon as mesoscopic spectral modulation (MSM) [III]. The MSM effect as a manifestation of two-mode interference has been experimentally demonstrated already more than a decade ago [26]: the two-mode operation of a specially fabricated step-index optical fiber (with ~4 μm core diameter) was achieved by exciting it with a light of just below the cut-off wavelength.

In our work [III] the MSM effect has been demonstrated for the light transmitted by an ordinary multimode optical fiber terminated by a metal-coated tapered tip with subwavelength aperture – a "SNOM tip" analogous to those used in scanning near-field optical microscopy (SNOM). In our case, the number of transmitted modes is limited by the mode-filtering ability of a SNOM tip [27]. Although in our original MSM work [III] we referred to OPD as "the phase shift τ", it was soon realized that such definition can be a bit confusing if taking into account that actual OPD values exceed the light's electromagnetic wave period by orders of magnitude, thus the corresponding phase shifts similarly exceed 2π. [IV]

It can be shown [25] that in the case of a two-mode optical waveguide a sinusoidal spectral modulation with frequency equal to OPD between the two modes is present at the exit. Thus the MSM effect can be used to obtain such an OPD value and to study the related intermodal dispersion for a certain waveguide sample. When using a multimode optical fiber terminated by a SNOM tip, one can expect that for a certain tip output aperture diameter a spectral interval exists, in which only two photonic modes (apparently HE_{11} and TM_{01} modes [27]) can be transmitted with significant and comparable amplitudes; this region can be identified by observation of a highly regular spectral modulation.

An MSM-based experimental technique for investigation of intermodal dispersion features in a metal-coated SNOM tip and in its multimode fiber tail has been proposed and realized [III]. This technique assumes performing a series of spectral measurements while gradually shortening the fiber tail. A linear OPD dependence on the fiber tail length l is expected due to the presumable uniformity of the fiber inherent intermodal dispersion along the fiber length. By extrapolating such a linear $\tau(l)$ dependence (obtained by fitting the experimental points) to $l = 0$ one can obtain a residual $\tau(0)$ value, which corresponds to the OPD generated by a merely ~1 mm long SNOM tip. We apply our MSM-based experimental technique to investigate an intermodal dispersion in several SNOM tips with Cr/Al coating and to test the hypothesis, according to which such dispersion can be affected by mode-selective coupling of photons to surface plasmon polaritons (SPP) of the metal coating. [III–V]

2. THEORETICAL BACKGROUND

2.1. Properties of NV centers

Nitrogen-vacancy centers (NV centers, see the structure in Fig. 1) are among the most common of the numerous types of point defects in diamonds. These centers are often found in nitrogen-rich type Ib diamond samples being subjected to irradiation damage. The center's most explored and useful property is its photoluminescence, which can be easily detected even from an individual NV center (typical spectra are shown in Fig. 2), especially for those in the negative charge state (NV^{-}). The emission consists of a broad vibronic sideband and of a narrow zero-phonon line (ZPL) at $\lambda \approx 637$ nm (1.945 eV) [28, 29], which is visible even at RT. See also chapter 5.2.

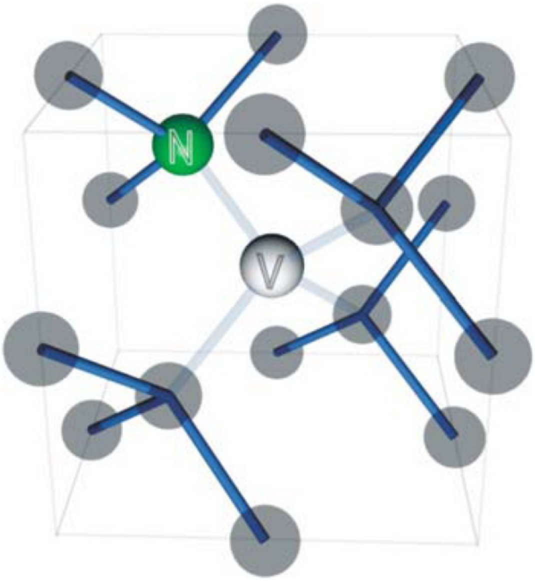

Figure 1: Schematic of the nitrogen vacancy (NV) center structure in diamond lattice [28].

Electron spins at NV centers, localized on atomic scale, can be manipulated at RT by applying magnetic field, electric field, microwave radiation, light, or a combination of those, resulting in sharp spectral and temporal resonances in the photoluminescence. These resonances can be explained in terms of electron spin-related phenomena such as quantum entanglement, spin-orbit interaction and Rabi oscillations, and analyzed using an advanced quantum optics theory. [28, 30] An individual NV center can be viewed as a basic unit of a quantum computer; it has potential applications in novel fields in electronics and computer science, including quantum cryptography and spintronics.

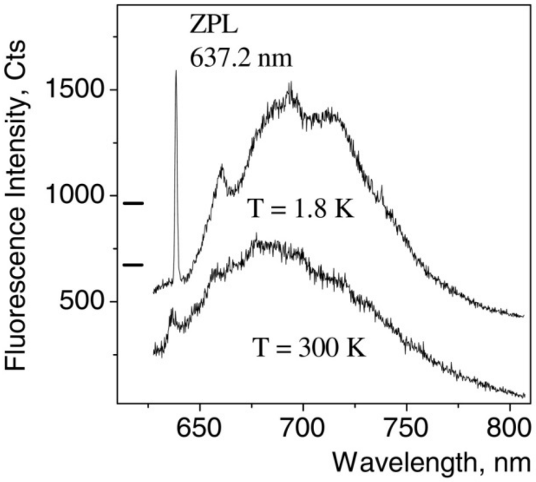

Figure 2: Sample fluorescence emission spectra of single NV centers at RT and at liquid He temperature. Excitation wavelength: $\lambda = 514$ nm. [28]

2.2. Properties of SiV centers

SiV centers are not found in natural diamonds. Defects with ZPL at 737 nm (1.68 eV) were first observed in cathodoluminescence (CL) investigations of homoepitaxial diamond layers and polycrystalline films grown on silicon substrates. [31] In 1981, a sharp 1.68-eV line in a spectrum of silicon ion-implanted diamond was observed by CL-spectroscopy. [32] The quadratic dependence of this CL line intensity on the ion dose has led to a hypothesis that a kind of Si_2 color centers is produced by Si ion implantation. However, in result of the ion implantation procedure other kinds of defects are produced as well, including the neutral vacancy with a similar wavelength of ZPL, thus resulting in an ambiguity.

However, in 1995 the mentioned ZPL has been at low temperatures resolved to 12 separate lines, which are grouped in 3 subgroups each consisting of 4 lines [33]. The relative strengths of the optical absorption for these 3 subgroups are found to have the same ratio as the abundances of the 3 natural isotopes of silicon: ^{28}Si, ^{29}Si, and ^{30}Si. This indicates that Si atoms are related to the 1.68-eV ZPL. The corresponding defects were then identified as SiV centers, taking into account that diamonds with Si impurities do not exhibit these fluorescence lines unless they have been bombarded with electrons and heated to at least 600° C, which indicates involvement of vacancies.

Polarized luminescence measurements have shown that SiV centers have <110> symmetry axes [34]. Theoretical calculations predict a model with a single Si atom and a neighboring vacancy site [35]. It is energetically unfavorable for a Si atom to occupy a carbon atom lattice position, thus it has to lay at an interstitial lattice position. Consequently, in this configuration a Si atom lays in the center of a kind of double-vacancy position, as shown schematically in Fig. 3.

This model is able to explain the doublet structure of the ground and the excited states and also delivers a theoretical value of the transition energy, which is close to the experimentally observed value (an energy scheme [33] proposed on the basis of four different lines within a subgroup is shown in Fig. 4). In addition, the model predicts a high stability and a 3-ns lifetime for the excited state, which is also in agreement with experimental results.

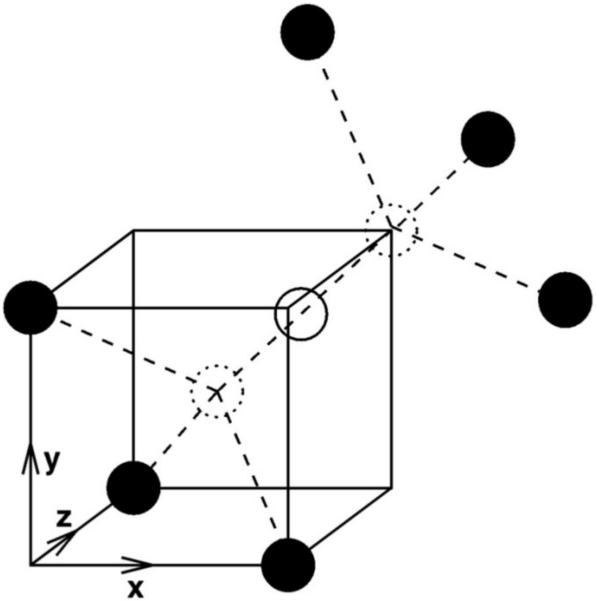

Figure 3: Schematic representation of the relaxed split-vacancy geometry of the SiV complex. The solid circles represent C atoms, the empty circle – the relaxed Si site, and the dashed circles – the diamond lattice sites. [35]

CL experiments at high temperatures have shown that SiV centers remain stable up to 1350º C [36]. Measurements of the center fluorescence in diamonds grown by chemical vapor deposition (CVD) yield lifetimes between 1 and 4 ns for different temperatures and diamond qualities [37]. On the ground of these findings, the theoretical energy scheme model (Fig. 4) describes a SiV center quite well. For application in single photon sources, the fluorescence spectrum and the radiative transition rate are of interest.

According to the described theoretical configuration of a SiV center, a Si atom has no direct binding to the diamond lattice. Therefore the center couples only weakly to the diamond phonons. This results in an RT fluorescence spectrum with a sharp 10 nm wide ZPL and a very weak vibronic side band.

However, most of the other types of color centers in diamond have a wide-band fluorescence spectrum (in Fig. 5, typical SiV and NV RT emission spectra are shown for comparison). The 4-ns excited state lifetime is also unusually short (e.g. NV centers have a lifetime of 13 ns), which makes the SiV center a very good candidate for application in a high-repetition-rate single photon source [38].

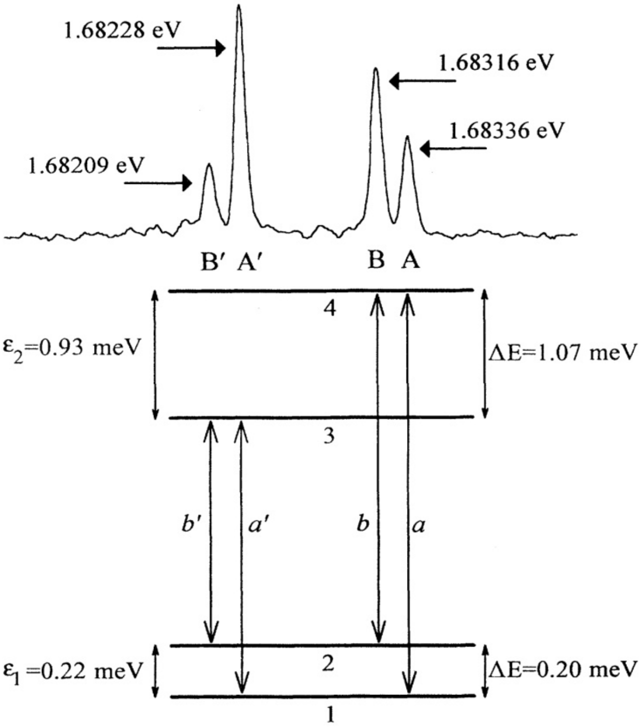

Figure 4: An energy-level diagram for a SiV center proposed on the basis of four different lines within a subgroup corresponding to the ^{28}Si defect center. [33] Since the splittings of the ground and excited states are very small, these fine structures cannot be observed at RT.

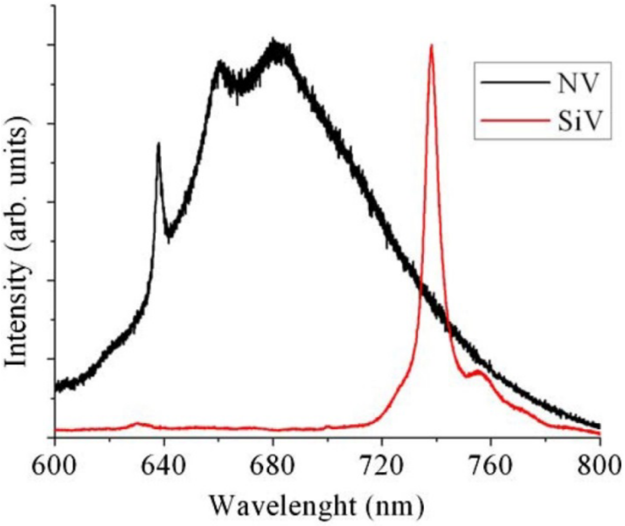

Figure 5: Typical RT emission spectra of SiV centers (observed in CVD nanodiamonds) and (for comparison) of NV centers. [39]

2.3. Surface plasmon polaritons

At certain conditions, optical photons can couple to specific excitations called surface plasmon polaritons (SPPs), which are able to propagate along a metal-dielectric interface. [40] These excitations involve both the collective motion of charged electrons in the metal ("surface plasmons") and the electromagnetic waves in the air or another dielectric ("polaritons"), and can be excited by both electrons and photons. [41] To excite an SPP with a photon of the same frequency, the wave vectors of both have to match. Due to their significantly shorter wavelengths, SPPs have promising applications, e.g. in future photonic (or plasmonic) nanochips. [42, 43]

An SPP wave propagating in x direction along a planar metal-dielectric interface is shown schematically in Fig. 6. The electric field of such a TM-polarized wave can be expressed as:

$$E = E_0 \exp[i(k_x x + k_z z - \omega t)], \tag{2.1}$$

where k is the wave number and ω is the frequency of the wave. The wave vector k_x of the longitudinal oscillation is tied to its frequency by a dispersion relation $\omega(k_x)$.

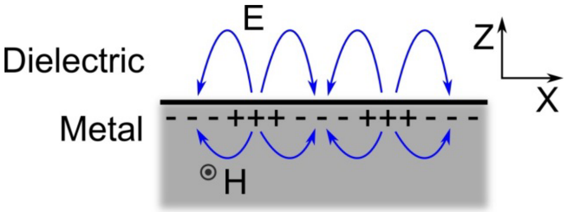

Figure 6: Schematic representation of a transverse magnetic (TM-polarized) electromagnetic wave propagating in x direction along a planar dielectric-metal interface and representing SPPs. The mixed (transversal and longitudinal) electric field E decreases exponentially in both positive and negative z directions perpendicular to the interface surface. The magnetic field H is directed along y.

The following continuity relations can be used to derive the dispersion relation for SPPs [44]:

$$\begin{cases} E_{xm} = E_{xd} \\ H_{ym} = H_{yd} \\ \varepsilon_m E_{zm} = \varepsilon_d E_{zd} \end{cases}, \tag{2.2}$$

where E is electric field, H – magnetic field, m denotes metal, d – dielectric; x,y,z – three orthogonal directions as shown in Fig. 6. The continuity of the wave vector k_x also fallows from Eqs. (2.2): $k_{xm} = k_{xd} = k_x$. Application of Maxwell equations yields the following relation [44]:

$$\frac{k_{zm}}{\varepsilon_m} + \frac{k_{zd}}{\varepsilon_d} = 0\,, \tag{2.3}$$

where ε_d is the electric permittivity of dielectric and $\varepsilon_m = 1 - \omega_p^2/\omega^2$ is that of the metal, ω_p – the bulk plasmon frequency of this metal. For any electromagnetic wave in medium i (i.e. m or d), we have:

$$k^2 = \varepsilon_i(\omega/c)^2 = k_x^2 + k_{zi}^2, \tag{2.4}$$

where c is the speed of light in vacuum. Combining Eqs. (2.3) and (2.4) yields the dispersion relation for SPPs [44]:

$$k_x = \frac{\omega}{c}\sqrt{\frac{\varepsilon_m\varepsilon_d}{\varepsilon_m+\varepsilon_d}}. \tag{2.5}$$

An example of SPP dispersion curve is depicted in Fig. 7 along with a conventional photon dispersion curve.

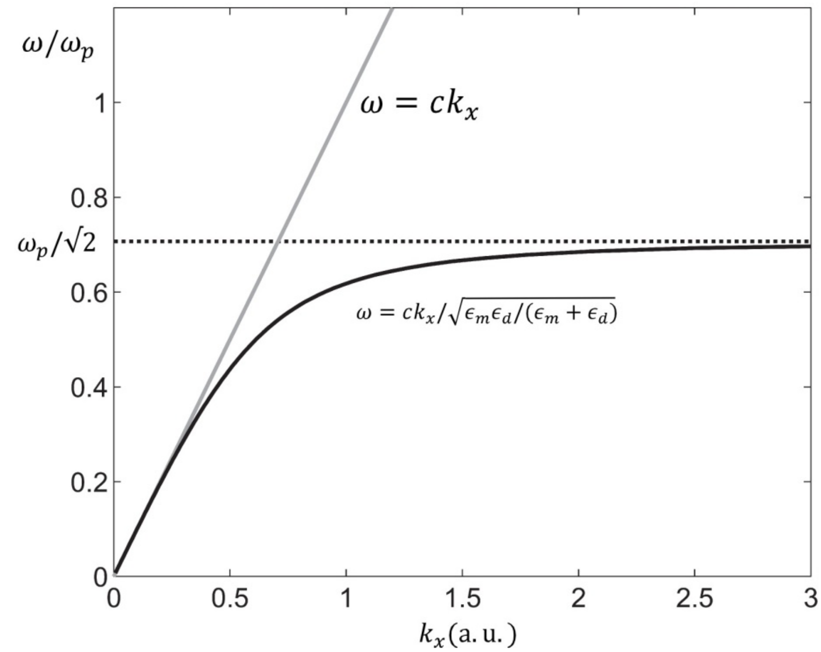

Figure 7: An example of SPP dispersion curve (black line) for an air as a dielectric with $\varepsilon_d \approx 1$. A conventional linear dispersion curve for photons is shown for comparison (gray line). The dotted line indicates the surface plasma frequency ω_{sp}. Adapted from [45].

At low frequencies SPP behaves like a photon, but when k is increased the SPP frequency approaches asymptotically its highest limit $\omega_{sp} = \omega_p/\sqrt{1+\varepsilon_d}$, which is called surface plasma frequency. The case of an air as a dielectric with $\varepsilon_d \approx 1$ is displayed in Fig. 7. For the low-frequency case $\omega \ll \omega_p$, one can obtain:

$$k_x = \frac{\omega n_m(\omega)}{c} \approx \frac{\omega n_d}{c}\left(1 + \frac{n_d^2\omega^2}{2\omega_p^2}\right), \tag{2.6}$$

where n_i denotes the refractive index of corresponding medium i. Thus we have the following relation for low-frequency SPPs in the case of a planar metal-dielectric interface:

$$\frac{n_m(\omega)}{n_d} - 1 \approx \frac{n_d^2\omega^2}{2\omega_p^2}. \tag{2.7}$$

If the metal-dielectric interface deviates from the planar configuration, the relation (2.7) should be considered as a coarse approximation. The $n_d^2\omega^2/2\omega_p^2$ -type frequency dependence of the quantity $n_m(\omega)/n_d - 1$ is universal for

$\omega \ll \omega_p$ and should still be present, but an additional numerical factor can apply, resulting in a modified relation [IV, V]:

$$\frac{n_m(\omega)}{n_d} - 1 \approx \alpha \frac{n_d^2 \omega^2}{2\omega_p^2} \tag{2.8}$$

It can be considered that the numerical factor α should not remarkably differ from unity if the curvature radius of the metal-dielectric interface surface significantly exceeds the wavelength of light λ. We use Eq. (2.8) to analyze our experimental results obtained with a metal-coated tapered tip of an optical fiber (see chapter 5.3).

3. EXPERIMENTAL

Several experimental setups have been designed, constructed and used in our work. In our early experiments [a, II], a fluorescence microscope was applied. The design enabled wide-field excitation for fluorescence (single-molecule) imaging, as well as spectral measurements from a small spot. But switching between different measurement modes was complicated and inefficient. For our SiV center-related work [I], a horizontal scanning microscope was constructed. With this setup, it was easy to measure the emission spectra originating from a tiny spot, to scan over a sample (film) surface, and to use the Hanbury Brown and Twiss interferometry [46]. A dedicated optical setup was constructed for our MSM-related experiments [III, IV]. A photo in the Extras (see Fig. 30) illustrates some practical design principles used in our optical setups.

3.1. Single-molecule imaging setup

The main difference of our experimental setup built for wide-field epifluorescence microscopy [47] from the setup recommended in the literature [48] is the use of an upverted microscope (Olympus MX14). One can use a cryostat for low-temperature measurements or an oil objective for achieving a higher NA. Most of the measurements were performed at room temperature using an air (not immersion) microscope objective with a relatively low NA (Edmunds, 60x magnification, NA = 0.9). Some later measurements have been accomplished using an oil immersion objective (Olympus, 100x magnification, NA = 1.4). A Newton EMCCD (CCD with electron multiplication on the chip) camera (Andor, matrix area 400x1600, pixel size 16 μm) was used as an imaging device. The EMCCD technology allows reducing the CCD readout noise in case of very low signals. The readout speed limits the time resolution to 0.1 s. To avoid an exposure during the CCD readout, an electromechanical shutter was installed in front of the camera. Commonly used exposure times were between 1 and 5 s; up to 200 frame movies have been recorded.

The frequency-doubled radiation (λ = 532 nm) of a CW Nd:YAG laser VA-532 (Viasho) was used for excitation. The linearly polarized laser beam was expanded by a telescope and reflected by a dichroic mirror into the microscope objective. The telescope lenses were adjusted to focus the excitation beam onto the back-focal plane of the microscope objective, creating on the sample an illuminated area of about 40 μm in diameter. The sample fluorescence was collected by the microscope objective and transmitted through the dichroic mirror. The backscattered laser light was blocked by a holographic Super Notch filter HSPF-532.0-1.0 (Kaiser) and an orange long-pass glass filer. After passing through the filters, the fluorescence was imaged onto the CCD camera by a 200-mm achromatic lens system. Eventually, a pixel of the camera image corresponds to a distance of 105 nm on the sample. A specific computer program was created to analyze the fluorescence kinetics of many individual molecules registered in a single movie.

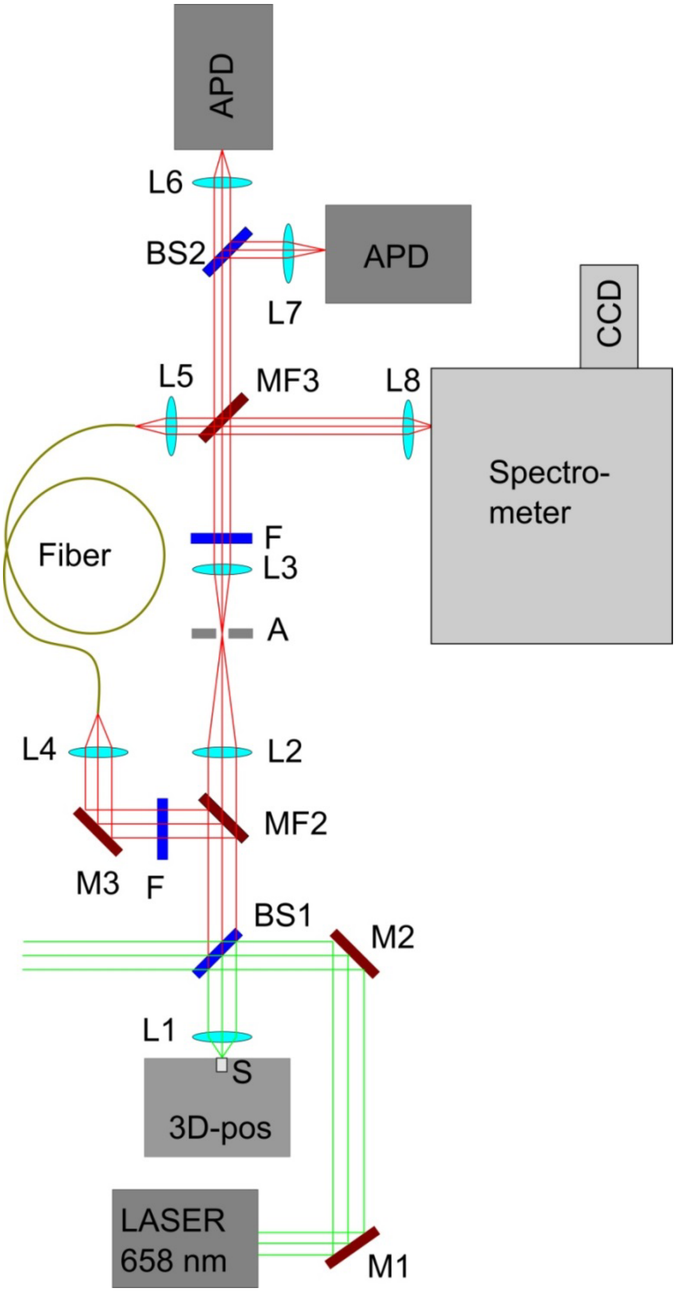

Figure 8: Optical scheme of our experimental setup designed for scanning microscopy and Hanbury Brown & Twiss interferometry. Green lines designate the ~658 nm excitation laser radiation, red lines – the secondary emission. 3D-pos – 3D (XYZ) positioner, S – sample (thin film), APD – avalanche photodiodes, L – lenses, A – aperture, F – filters, M – mirrors, MF – flippable mirrors, BS – beam splitters. Fiber – an optional multimode optical fiber, used in MSM experiments.

3.2. Scanning microscopy and Hanbury Brown & Twiss interferometry

A schematic of our related experimental setup is presented in Fig. 8. A homemade confocal microscope equipped with a XYZ motorized scanning stage (3D positioner) was used for spatial micromapping and localization of bright optical emitters in thin films. The emission of a laser diode operating at 658 nm was used for optical excitation. Using this excitation wavelength was motivated by the need to eliminate the possible photoluminescence background originating from NV centers. The luminescence from the confocal volume was either split into two parts and detected by two avalanche photodiodes (APD) for correlation measurements or sent to a single-grating spectrometer (Shamrock i301 equipped with Newton EMCCD) to perform spectral measurements. The APDs were configured as a Hanbury Brown and Twiss interferometer used for the emission characterization needed to evaluate the number of single quantum emitters active in a selected nanoisland. The scattered laser radiation was blocked by an interference edge filter (red-pass from 664 nm, Semrock LP02-664RS-25) while the useful fluorescence was selected by a red narrow-bandpass interference filter. An example of obtained second order correlation function is shown in the Extras (Fig. 31).

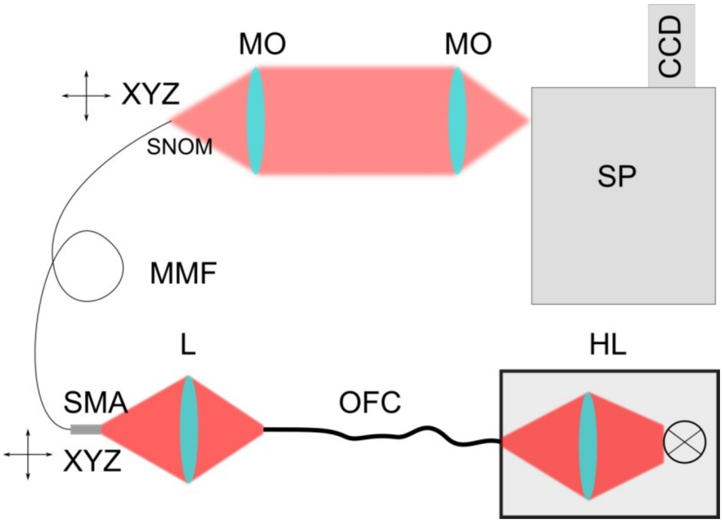

Figure 9: Optical scheme of our second MSM experimental setup. HL – 150 W halogen lamp coupled in a high-intensity illuminator to a 3 mm output diameter optical fiber cable (OFC); MMF – multimode optical fiber of length *l* terminated at the input by an SMA connector and at the rear end – by a SNOM tip, positions of the both terminals can be adjusted by (XYZ) 3d micrometric translation stages; MO – microscope objectives used to couple the SNOM output light into the spectrometer SP equipped with a CCD camera; L – focusing lens coupling OFC output to MMF input (see Fig. 10).

3.3. Fiber-related experiments

In our first MSM experiments [III], the described optical setup was, as shown in Fig. 8, adapted to enable exciting of a multimode optical fiber with the fluorescence of SiV centers embedded in a thin film of ultra-nanocrystalline diamond [49] deposited on a Si substrate, while collecting the radiation from the fiber's output terminal.

In our subsequent MSM experiments [IV, V], a new optical scheme was used to excite the multimode optical fiber, as shown in Fig. 9. In addition to introducing a halogen lamp as a broadband light source, the new setup also enabled experiments with shorter fibers. A 150 W halogen lamp was used as a source of the broadband light. The lamp is installed in a high-intensity illuminator MI-150 (Dolen-Jenner), which couples it to a 3 mm output diameter optical fiber cable. After passing through an optional red-pass filter the radiation from the optical cable output was focused by a 13.86 mm focal length lens to a ~1.5 mm diameter "spot", within which an input face of the multimode optical fiber was positioned. This "focused light spot" should be understood as the light field formed by the focusing lens in the image plane of the optical cable output face.

The excitation of a multimode fiber tail is in more details schematically explained in Fig. 10. The position of multimode fiber input face can be laterally adjusted within the much broader "light spot". This fiber of length *l* plays the role of an input tail for a SNOM tip. The light transmitted by a SNOM tip is collected paraxially in the far zone by a microscope objective (Zeiss Achroplan, 32x magnification, NA = 0.4) and directed using another objective into a Shamrock SR-303i spectrograph coupled to a Newton CCD camera (both Andor).

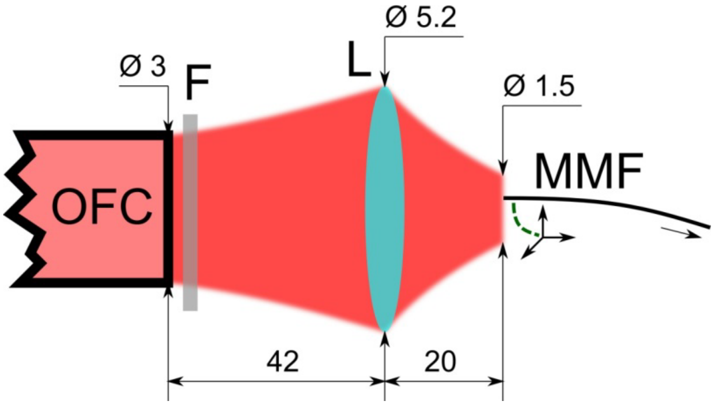

Figure 10: Schematic explanation of the excitation of multimode optical fiber (MMF) by the broadband light from optical fiber cable (OFC). The radiation is focused by a 13.86 mm focal length lens (L) to a ~1.5 mm diameter "spot" in the transverse (image) plane, which contains the input face of MMF (the cladding outer diameter is 125 μm) with laterally adjustable position within this plane. F – an optional red-pass filter. All dimensions are in millimeters.

We used Al-coated 200 nm, 150 nm and 100 nm (output aperture diameter) SNOM tips produced by Nanonics Imaging Ltd (Jerusalem) as bent-type SuperSensor™ NSOM/AFM Probes: about 0.6 mm long tapered tip of the multimode fiber is coated with metal layers of Cr and Al with respective thicknesses of ~20 and ~200 nm. A microscopic image of the 200 nm SNOM tip is presented in the Extras (see Fig. 32). The step-index fused silica fiber tail has core and cladding diameters of respectively $a_1 \approx 50$ μm and $a_2 \approx 125$ μm; the refractive index of the core (n_1) exceeds that of the cladding ($n_2 \approx 1.453$ for $\lambda \approx 800$ nm) by about 1%. The fiber probe bend is located in a fiber region close to the tapered tip; the bending radius exceeds the light wavelength by at least an order of magnitude, thus the bend should not significantly affect the mode structure of the transmitted light. An input face of the fiber tail was formed by polishing (finished using 1 μm lapping film) and equipped with an SMA-type connector each time after reducing the tail length. Positions of the fiber terminals – the SMA connector at the input and the SNOM tip at the output – were both adjustable with 3d micrometric translation stages.

4. GOALS OF THE STUDY

The following goals have been set for our experimental study:

1. Participation in finding methods for preparation of nanosized diamond particles containing a single or few emitting SiV centers and of diamond nanofilms with correspondingly low concentration of such centers. Optical and spectroscopic investigation of obtained samples with sub-lambda spatial resolution.
2. Spectroscopic and Raman investigation of nanosized diamonds, which contain emitting NV centers.
3. Study of light propagation in optical waveguides and in nanofibers with sub-wavelength features. Investigating effects of a tapered metal-coated optical fiber terminated by a sub-wavelength aperture (a "SNOM tip") on the spectrum of the transmitted light and spectral effects of intermodal interference.
4. Development of an experimental technique allowing investigation of the relative value of modal dispersion for a certain pair of fiber modes, separately in the fiber tail and in the SNOM tip.
5. Looking for the effects of photon-plasmon coupling in a metal-coated SNOM tip on spectral properties of transmitted light.

5. RESULTS AND DISCUSSION

5.1. Preparation and spectroscopic study of SiV center-based emitters [I]

From reviews concerning optical defects in diamonds [10, 11] we can conclude that the most stable and promising for single emitter applications are NV and SiV centers. SiV center is almost an example of ideal single-photon emitter. Indeed, even at RT the spectrum of SiV centers consists of a zero-phonon line at 738 nm and a weak phonon sideband. The luminescence lifetime is quite short, ~1–4 ns [37]. An ion implantation of IIa diamonds was initially used to produce single SiV emitters [13]. Yet, this technique is quite expensive and requires post-implantation annealing in vacuum at 1000º C.

In cooperation with our colleagues from General Physics Institute (Moscow) we elaborated a CVD-based technique of diamond film preparation. Nanocrystalline diamond films were grown in microwave plasma reactor on mirror-polished Si substrate. Before the deposition the substrate was seeded with ultradispersed diamond (UDD) clusters of detonation synthesis using a special aerosol-plasma technique. The silicon doping of diamond was realized through the substrate chemical etching in the plasma at the first stage of the deposition process (when the diamond film still remains island-like): Si atoms and/or SiHx species are incorporated from plasma to growing crystallites. To get a thin diamond film containing SiV centers, the following parameters were chosen: substrate temperature 850º C, pressure 87 Torr, gas flow rate 500 sccm, microwave power 3.4 kW, and deposition time 3 min. It can be concluded from SEM images (an example is shown in Fig. 11) that we have an island-like diamond film surface.

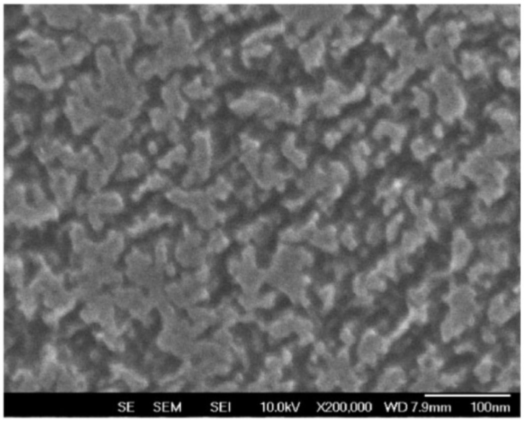

Figure 11: A SEM image of nanodiamond film doped with SiV defects. The film was produced by CVD technique in a microwave plasma reactor.

The Renishaw micro-Raman/luminescence spectrometer was applied for optical characterization of the samples using both the microluminescence and Raman techniques. Spatial micromapping and separation of bright optical emitters in the films was performed using a homemade confocal microscope equipped with an XYZ motorized scanning stage. In addition to the 488 nm Ar+ laser line, the emission of a 658 nm laser diode was also used for optical excitation, which enabled the elimination of probable photoluminescence (PL) background originating from NV centers.

Probing of PL with a 488 nm laser beam of ≈1 µm diameter in different points of the island film surface revealed a micrometer-scale nonuniformity of the distribution of PL emission intensity from SiV centers. There were few-micrometers-sized regions with no SiV emission at all, whereas within other similar-sized regions the intensity of SiV emission varied in a few times from point to point. Combined Raman/PL spectra of the film with the strongest signal from SiV centers (with excitation at 488 nm) are shown in Fig. 12.

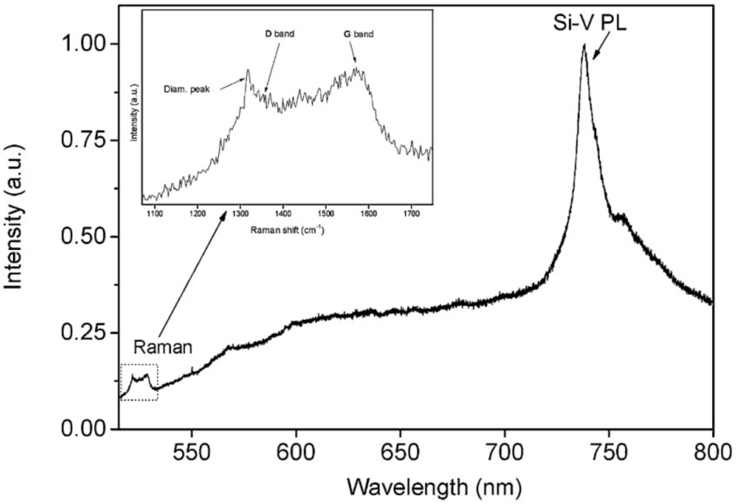

Figure 12: Combined Raman/PL spectra of a CVD nanodiamond film, measured at RT. (Excitation: 488 nm).

We can conclude that the Raman spectrum of the nanodiamond film consists of three lines indicating the presence of diamond (the narrow peak at 1332 cm^{-1}) and amorphous carbon (two broad bands at 1350 cm^{-1} (D) and 1570 cm^{-1} (G)). The PL spectrum shows only the doublet of zero-phonon line from SiV centers at 738 and 757 nm. Note the absence of 575 and 638 nm lines related to NV centers in the ≈20 nm thick nanocrystalline diamond film. To investigate in more detail the spatial distribution of fluorescence intensity in the spectral range of maximum SiV emission, the confocal PL mapping was performed with 658 nm laser excitation. The narrow-spectral-range fluorescence was selected by a red bandpass filter (Omega Optical 3RD720-760) with central wavelength at 740 nm and 40 nm bandwidth. The mapping image is shown in Fig. 13.

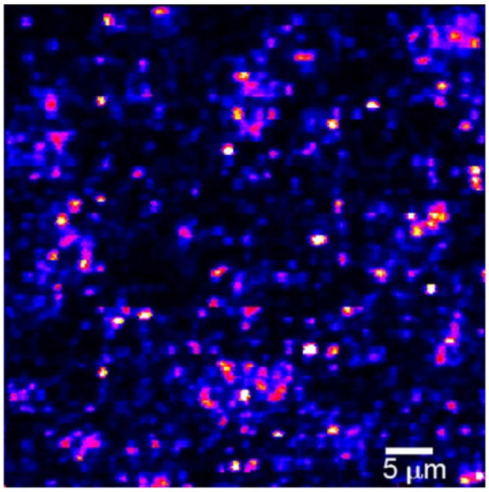

Figure 13: An image of confocal fluorescence mapping of CVD nanodiamond film with 658 nm laser excitation, at RT. The fluorescence is selected by a red bandpass filter (center wavelength 740 nm, bandwidth 40 nm). Blue–red–white is a color sequence corresponding to the increase of emission intensity.

The distribution of emission intensity around 738 nm is similar to that observed with 488 nm laser excitation, as described above. The image consists of few-micrometer-sized regions, part of which do not exhibit any emission at 738 nm, but others demonstrate an emission of variable intensity within a region. Note that besides the expected emission from SiV centers the Raman scattering from amorphous carbon (G line) was also contributing into the bright emission shown in Fig. 13.

Typical PL spectra from two different spots recorded without any bandpass filter with 658 nm laser excitation are shown in Fig. 14. The 738 nm line from SiV centers dominates in the filter bandpass region of the upper PL spectrum, while the G band of amorphous carbon dominates in this region of the lower PL spectrum (Fig. 14). The first and the second order silicon Raman lines (520.5 and 963 cm^{-1}, respectively) coming from the substrate are also present in both spectra in Fig. 14. A substantial quantity of non-diamond carbon is a characteristic feature of the initial stage of CVD diamond growth [50]. Positions of PL image bright spots associated with a strong amorphous carbon signal (G band) demonstrate the high nonuniformity of the amorphous carbon distribution within the nanodiamond film on a micron scale.

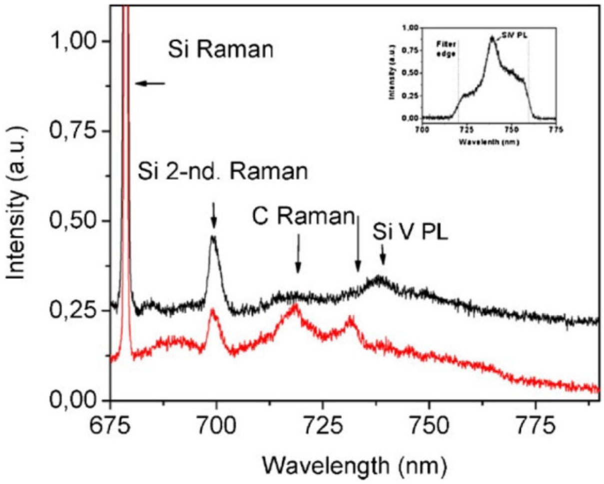

Figure 14: Emission spectra taken at RT under 658 nm excitation from three different bright spots on a nanodiamond sample. Raman lines from silicon substrate are designated as Si and Si 2-nd (520.5 and 963 cm^{-1}, respectively). Carbon Raman bands at 1350 and 1580 cm^{-1} are indicated as C Raman. Inset: the most characteristic SiV spectrum taken with a bandpass filter with central wavelength at 740 nm and a bandwidth of 40 nm (Omega Optical 3RD720-760). Dotted lines indicate the bandpass region of the filter.

We used the Hanbury Brown and Twiss interferometry to investigate the photon statistics of radiation from the SiV-related bright spots. It was found that this statistics is virtually a Poissonian one, which indicates the presence of multiple color centers in the laser focus. Two main factors could explain this result. The first one is the essential broadband structureless background observed in PL spectra obtained with 658 nm excitation (seen clearly in the inset of Fig. 14). Clarification of the origin of this background is in progress. Over the filter bandpass region the integral background emission intensity is about twice as high as the integral intensity of SiV emission. The second factor is the presence of several SiV defects within the laser probing volume of the film. The variable intensity of the emission from fluorescent regions confirms this assumption.

In conclusion: a spatial localization of the photoluminescent SiV centers in a thin (ca. 20 nm) CVD nanodiamond film, which was grown at high seeding density and doped with Si from the silicon substrate, was studied. It was found that in spite of the uniform highly-dense coating of the Si substrate with diamond nano-islands, at micrometer level the emission from SiV centers is not uniformly distributed over the film surface. Further study of the reasons of such nonuniformity is required. In fluorescent regions, the density of emitting centers is higher than one per μm^2.

5.2. Spectroscopic study of NV emitters in detonation nanodiamonds [II]

The most investigated color centers in diamond are NV centers, which have several promising applications. Being incorporated in nanodiamonds, such centers can be used e.g. as nontoxic fluorescent labels in biological systems [51]. A single NV defect is demonstrated to perform as an efficient single-photon source for future quantum computing applications [30]. Another fine application for a single NV center is found in nano-magnetometry [52].

A careful research was performed on growing, by using the CVD technique, of isolated diamond nanocrystallites containing single NV color centers. [53] A conclusion was made that an optimal size for such crystallites, which incorporate single optically active NV centers, is 60–70 nm. To produce nanodiamonds, the so-called top-down method is often used, which assumes grinding of high-pressure-high-temperature (HPHT) diamonds doped with a small amount of nitrogen atoms. In order to produce photoluminescent nanodiamonds from this material, the powder has to be irradiated with electrons to create vacancies. Subsequent annealing at 800º C leads to the formation of emitting NV centers (see e.g. Ref. [54]).

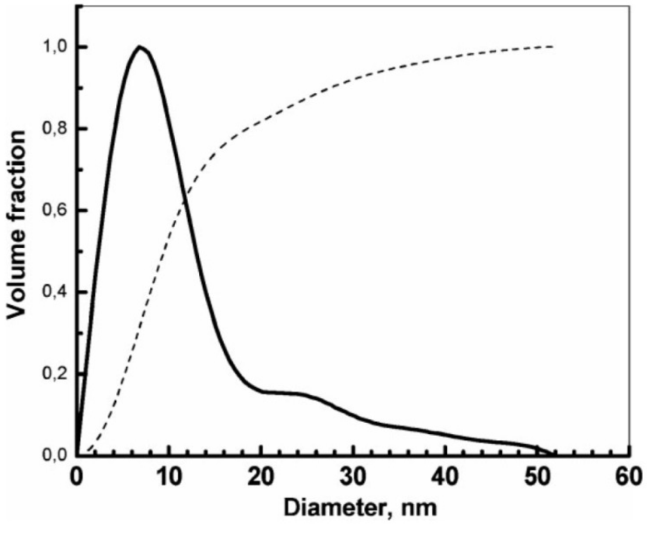

Figure 15: Size distribution (solid line) of the DND primary particles determined by SAXS. The main peak corresponds to grains of 6-nm diameter, and the tail of the size distribution spreads beyond 25 nm. The dashed curve shows the integrated size distribution, i.e. the volume fraction of DND primary particles with sizes below the certain diameter.

For our spectroscopic investigations we used differently produced, so-called detonation nanodiamonds. The preparation method is an alternative bottom-up approach for the large-scale nanodiamond synthesis. The synthesis of detonation nanodiamonds is based on the carbon-containing high-energy explosives (so called C-H-N-O explosives). The produced nanodiamonds have average primary particle sizes of approximately 3–6 nm, depending on the details of the synthesis, and possess a spherical/polyhedral shape. A small fraction with larger sizes is also typically present in the obtained detonation nanodiamond (DND) powder [55]. The size distribution of produced nanodiamond crystallites in the studied DND powder was analyzed by using the technique of small-angle X-ray scattering (SAXS); the resulting distribution (shown in Fig. 15) was obtained by assuming a spherical morphology using the Tikhonov's regularization method [56].

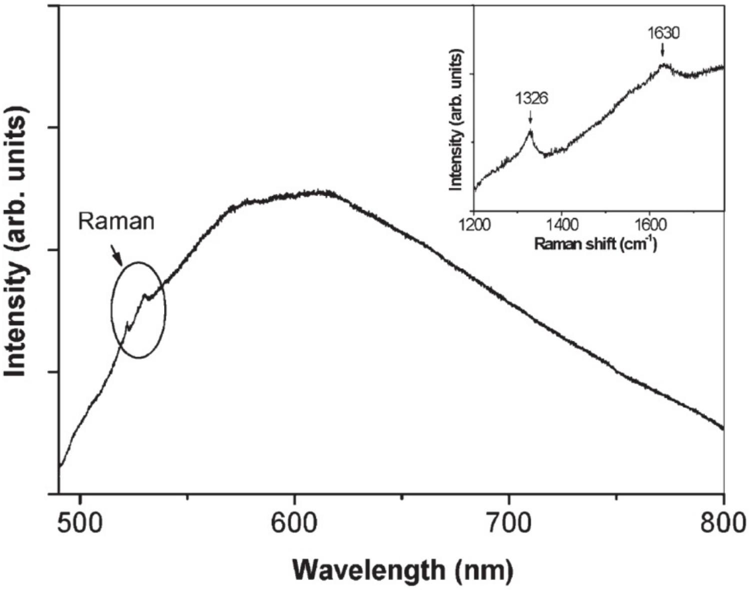

Figure 16: PL-Raman spectrum of DND powder measured at room temperature using a 488-nm excitation wavelength. The inset shows the Raman part of the spectrum in the range of 1200–1700 cm^{-1}. The PL spectrum presents a structureless broad band with a maximum around 600 nm. The Raman spectrum consists of the two lines at 1326 and 1630 cm^{-1} related to the vibrational modes of, respectively, diamond and sp^2-bonded carbon.

A PL-Raman spectrum taken from a thick (about 1mm) layer of the DND powder is shown in Fig. 16. The Raman part of the spectrum (shown in the inset) consists of two lines at 1326 and 1630 cm^{-1} related to the vibrational modes of, respectively, diamond and sp^2-bonded carbon. For large (micrometer-scale and larger) crystals the diamond Raman peak is normally positioned at 1332 cm^{-1}, corresponding to the phonon modes from the center of the Brillouin zone, and has a symmetric shape. For nanoscale-sized crystals the diamond peak is down-shifted from the 1332 cm^{-1} position and asymmetrically broadened with decreasing the crystal size due to the phonon confinement effect [57]. The position of the diamond Raman line at 1326 cm^{-1} should correspond to Raman scattering from the dominant fraction of 6-nm crystallites in the DND powder. The PL spectrum presents a structureless broad band with a maximum around 570 nm. As it was demonstrated [55, 58, 59], the characteristics of nano-diamond PL can be strongly varied by functionalizing the nanodiamond surface. Thus, the broad PL band is most likely related to emission from electron levels created in the diamond bandgap by surface defects. No essential changes in the PL-Raman spectrum of the thick DND layer took place after 2 MeV electron irradiation and 700º C annealing of this material.

When a thick layer of DND is used, the observed Raman and luminescence signals are expected to be mostly attributed to the main volume fraction of the diamond powder, consisting of approximately 6-nm crystallites. To increase the probability of detecting large diamond nanocrystals and to compare their PL spectra with those of 6-nm particles we applied the following procedure of DND sample preparation. The DND powder was dispersed in dimethyl sulfoxide (DMSO) and a thin DND layer was prepared on a Si substrate from this solution. A scanning electron microscopy (SEM) image of such a DND layer is shown in Fig. 17.

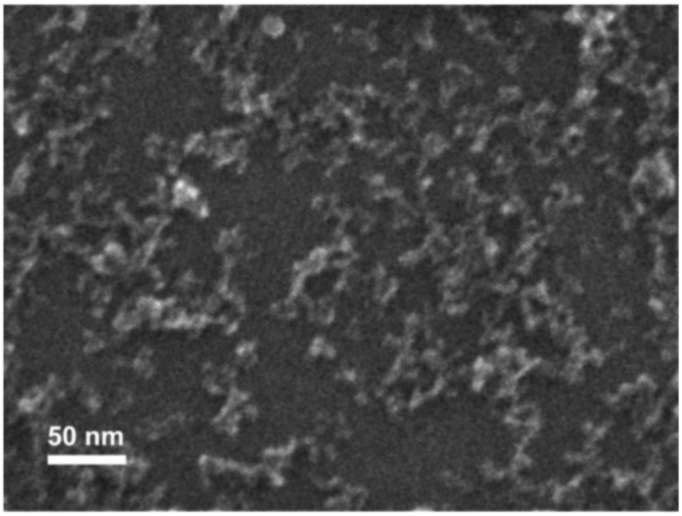

Figure 17: SEM image of DND crystallites dispersed on a Si substrate.

The estimated thickness of the produced DND island-like layer was on average less than 100 nm. This allows the PL measurement of large diamond crystallites while minimizing the interference from small crystallites. Prior to the optical study, the DND layer was electron-irradiated and annealed. To study the PL properties of the layer, a purpose-built PL-Raman spectroscopy system was used, working in 1) the image regime showing the integral PL intensity distribution within a large area of sample surface, or 2) the regime of confocal PL-Raman spectral measurements. Using the first regime in combination with an edge filter (transmitting the light with wavelengths >630 nm), an image of the photoemission from DND film surface illuminated with a 532 nm laser was obtained. This image, 53 µm × 37 µm in size, is shown in Fig. 18.

A number of bright spots is clearly visible. A typical PL and Raman spectrum measured in one of the bright spots using the second regime is shown in Fig. 19. Two lines at 575 and 638 nm, related to electron transitions at NV^o and NV^- defects are clearly visible in the spectrum. The diamond Raman line is detected in the unshifted 1332 cm^{-1} position, indicating that the bright emitting spots in Fig. 18 are related to large DND crystals. According to Ref. [60], a well-distinguishable down shift in the Raman position (about 2 cm^{-1}) from 1332 cm^{-1} is observable when the diamond particle size decreases below 30 nm. The lack of this shift in the Raman spectrum in Fig. 19 leads to the conclusion that the bright PL from NV centers is detected from DND crystallites with sizes above 30 nm. Besides the diamond Raman line, the first- and second-order Raman lines of sp^2-bonded carbon, and also the phonon sidebands of the NV^o and NV^- centers, are observed in the PL-Raman spectrum.

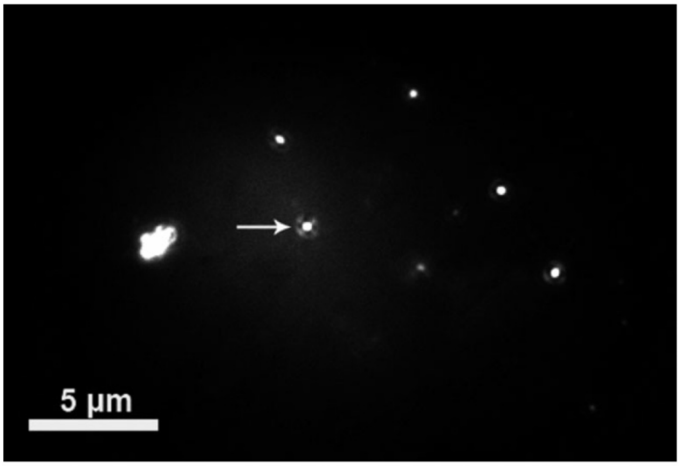

Figure 18: An image of the integral PL intensity distribution within a ~50 µm diameter spot of 532-nm laser excitation of DND crystallites dispersed on a Si substrate. The luminescence is selected by an edge filter transmitting light with wavelengths >630 nm. The PL spectrum of the bright spot indicated by the white arrow is shown in Fig. 19.

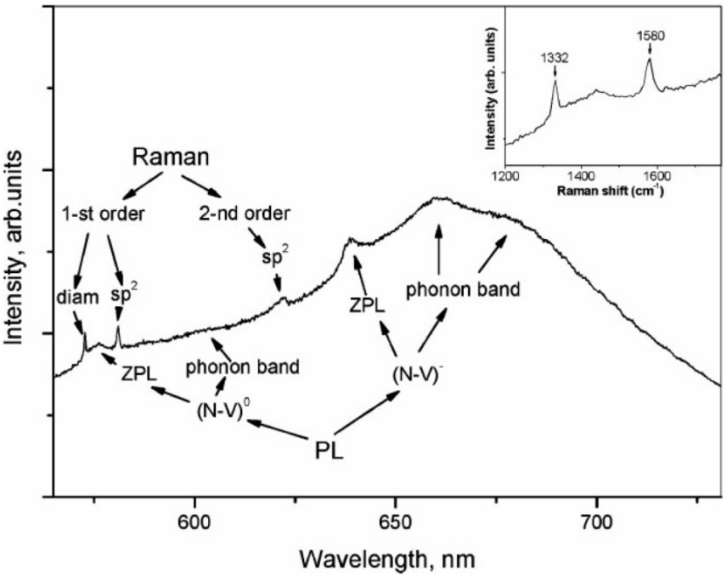

Figure 19: PL-Raman spectrum recorded at RT in the bright spot indicated by the white arrow in Fig. 18. The insert shows the Raman part of the spectrum in the range of 1200–1700 cm^{-1}. The excitation wavelength is 532 nm. The laser beam is focused in a spot of 1 μm diameter.

We can conclude that the examined explosion-produced nanodiamond (DND) powder contains a significant fraction of over 30 nm sized nanocrystallites, which demonstrate at 637 nm a well-pronounced zero-phonon line of NV$^-$ centers. This result suggests that the detonation technique can be used to manufacture optical nanodiamond markers with emitting NV centers.

5.3. Optical nanofibers: MSM-related studies and plasmonic effects in SNOM tips [III–V]

A series of nano-optics experiments has been initiated in order to investigate the effect of an optical fiber terminated by a SNOM tip with subwavelength output aperture on the transmitted light spectrum. In our first experiments we used a light source based on a diamond sample with SiV centers, which were excited by a strongly focused 532 nm or 658 nm laser radiation. [III] As shown in Fig. 20, the SiV room-temperature fluorescence zero-phonon line is about 9 nm broad (FWHM), centered at $\lambda \approx 738$ nm. The optical setup is schematically shown in Fig. 8. The SiV emission was collected by a confocal microscope and, after passing a red-pass filter, directed into a multimode optical fiber with an optional SNOM tip formed on its output end. We used Nanonics bent-type

SuperSensor™ NSOM/AFM Probes with output aperture diameters of 100 nm and 200 nm. The same type of multimode fiber with two identical ends (without any SNOM tip) has been used for comparison purposes. The light transmitted by the multimode fiber and an optional SNOM tip was collected by an objective and directed into a spectrograph (Andor Shamrock SR-303i).

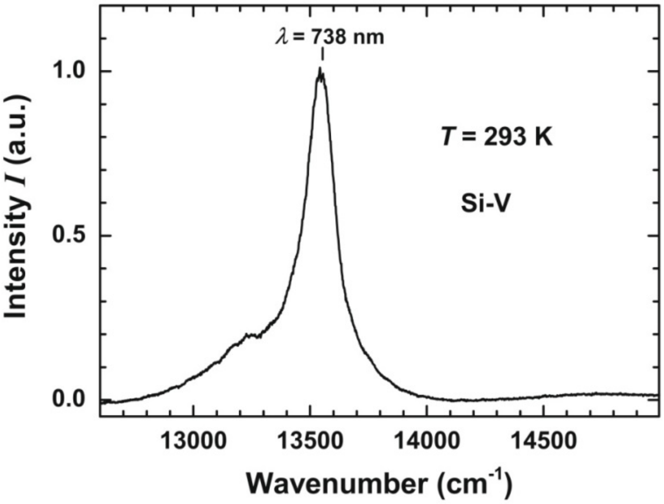

Figure 20: Room-temperature emission spectrum of silicon-vacancy (SiV) centers in diamond. The SiV fluorescence is excited by a strongly-focused 532 nm laser radiation, which is filtered out by a red-pass filter.

It has been demonstrated that under certain conditions a remarkable spectral modulation can be observed in the transmitted light. [III] This effect is of mesoscopic origin, occurring only for a certain interval of SNOM output aperture diameters (see Fig. 21). The MSM effect is actually enabled here due to the mode-filtering ability of a SNOM tip and to the inherent intermodal dispersion of a multimode fiber: a noticeable modulation appears when the number of transmitted fiber modes is small but exceeds unity.

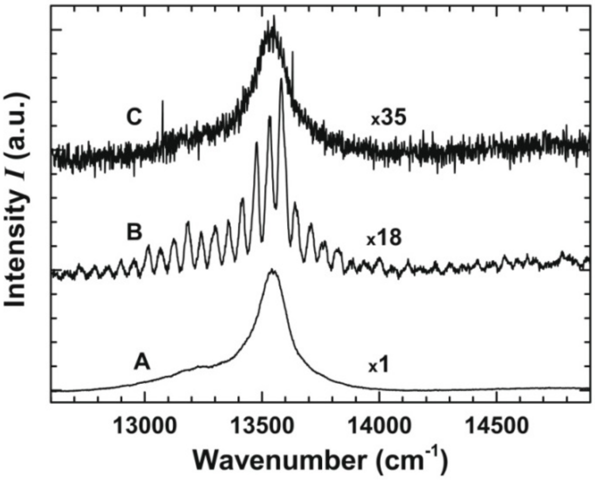

Figure 21: Spectra of SiV fluorescence transmitted by different multimode fiber samples. Baselines of the spectra are shifted for clarity; vertical scales are changed for an easier comparison. (A) An ordinary fiber (without a SNOM tip), signal collection time t_c = 180 s; (B) fiber terminated by a 200 nm SNOM tip, t_c = 900 s, vertical scale relative magnification ×18; (C) fiber terminated by a 100 nm SNOM tip, t_c = 27000 s, vertical scale relative magnification ×35.

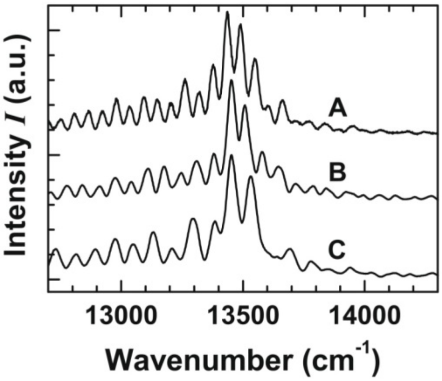

Figure 22: Spectra of SiV fluorescence (excited by 658 nm diode laser) transmitted by a multimode fiber terminated by a 200 nm SNOM tip, where the multimode fiber length l is gradually reduced: (A) l = 1.075 m; (B) l = 0.920 m; (C) l = 0.765 m. The baselines of spectra A and B are shifted for clarity.

We proposed and applied [III] an MSM-based experimental technique allowing, as already described in chapter 1.2, to separate the fiber tail and the SNOM tip contributions to the entire obtained OPD value. As can be seen in Fig. 22, the period of spectral modulation depends on the fiber tail length. However, it turned out that, due to the relatively narrow emission spectrum of the light source used [III], the precision of the results obtained using this technique was insufficient to reliably evaluate the relatively small OPD value generated by a SNOM tip. Changes had to be introduced to the experimental configuration in order to resolve this issue.

An optical scheme of our redesigned MSM experimental setup is shown in Fig. 9. In addition to introducing a halogen lamp as a broadband light source, the new setup also enables experiments with shorter fibers. The excitation of a multimode fiber tail is schematically explained in Fig. 10. [IV, V] The application of broadband excitation light allowed us to select (for every individual SNOM tip) a spectral region featuring highly regular spectral modulation in the transmitted light, which indicates the two-mode interference.

However, it appears that an exact spectral pattern measured depends actually on the lateral position of the multimode fiber input terminal (i.e. of the SMA connector) in the focal plane of exciting "light spot" (see Figs. 9, 10), being reproducibly sensitive to displacements as small as some micrometers (thus indicating the mesoscopic origin of such dependence). As can be seen from the sample spectra in Fig. 23, shapes and amplitudes of major interference maxima can vary, as well as distances between adjacent maxima. Weak (low visibility) modulation of different period can superimpose on the main modulation pattern at some SMA positions. We attribute these effects to variable nonzero contribution of other fiber modes, in addition to the two major modes.

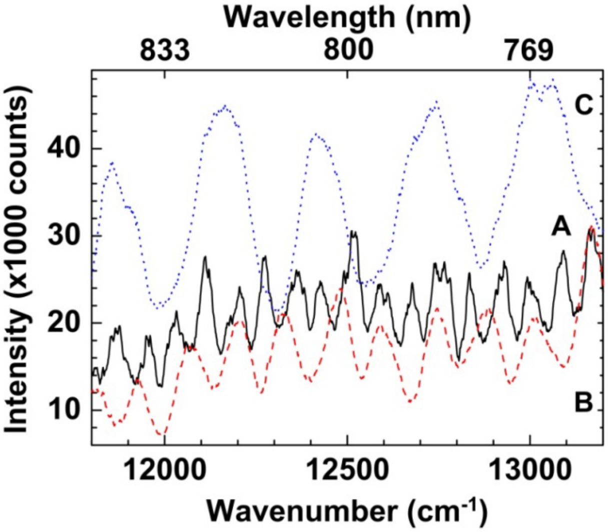

Figure 23: Three examples of spectral modulation observed with different fiber tail lengths *l*: (A, solid line) *l* = 769 mm; (B, dashed line) *l* = 479 mm; (C, dotted line) *l* = 240 mm. Signal collection time 300 s. Distinct signal levels are caused by nonidentical fiber input terminal (SMA) positions in the exciting "light spot" [IV]

It turns out that even in the selected spectral region the high-visibility regular modulation can be registered only for some specific SMA position range(s). This phenomenon can be tentatively explained by considering the requirement of coherent excitation of the two modes in order to be able to observe their interference [61]. Taking into account an obviously low degree of spatial coherence of our broadband light source and the complicacy of the exciting light field structure, it seems reasonable to assume that for some SMA positions the two major fiber modes are excited (at least partially) coherently, while for other positions they are excited non-coherently. For every fiber tail length *l* the spectra were measured with different SMA position adjustments till a "proper adjustment" enabling application of the two-mode model was found (see sample spectra in Fig. 24). According to the theory of optical fibers [27, 62–64], if the fiber diameter is gradually reduced, the last two remaining modes are HE_{11} and TM_{01}: in a conventional fiber without any metal coating the cutoff radius is the same for TM_{01} and TE_{01} modes being both referred as LP_{11} modes in the LP model [63, 64], yet in a metal-coated fiber this radius is smaller for TM_{01} mode [27].

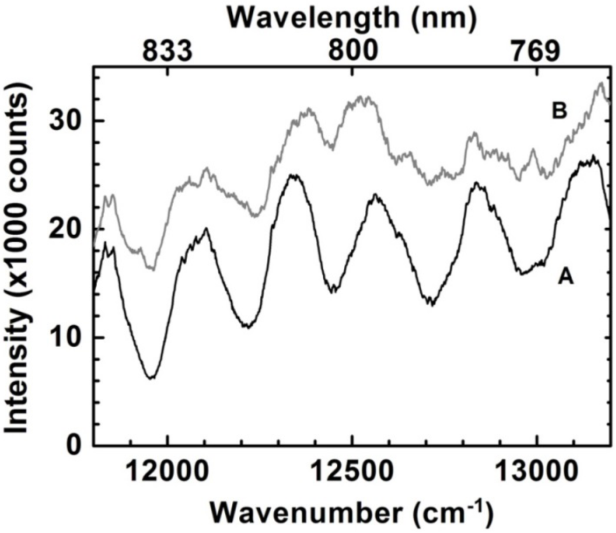

Figure 24: Two examples of spectra observed for the same fiber tail length (*l* = 273 mm) with different SMA position adjustments, which in addition to the signal level also affects the spectral modulation pattern. Spectra are obtained in cases of (A) "proper adjustment" (suitable for OPD study) and (B) "improper adjustment" of the SMA position – in the latter case the two-mode model cannot be properly applied. Signal collection time 300 s. [V]

According to the two-mode model [III, 25], OPD between the two major modes can be found as $\tau = 1/\Delta f$, where Δf is the period of spectral modulation in the frequency scale. Fitting the spectrum with a sine function could be a proper way of evaluating Δf (and OPD) in the case of negligible spectral dispersion, but due to the possible contribution of several factors such a case could not be presumed. Thus our choice was to estimate the spectral position of any major interference maximum separately, by fitting it with a Gaussian curve; any interference maxima with visibility lower than a preset threshold (e.g. 0.1 in the case of our 200 nm SNOM tip) were ignored. It appears that the fluctuations of individual peak positions tend to average out over a broader spectral interval. Such an averaging-out indicates that perturbations caused by small contributions of several modes with different phase velocities average out due to the differences of corresponding modulation periods, yet the regular oscillations caused by the interference of two major modes remain. Interestingly, in some cases a good linear regression fitting of the obtained peak positions can be performed over the whole chosen spectral interval (see examples in Fig. 25); in such a case a reliable average value of Δf and quite an accurate OPD value can be estimated, effective over the whole chosen spectral interval.

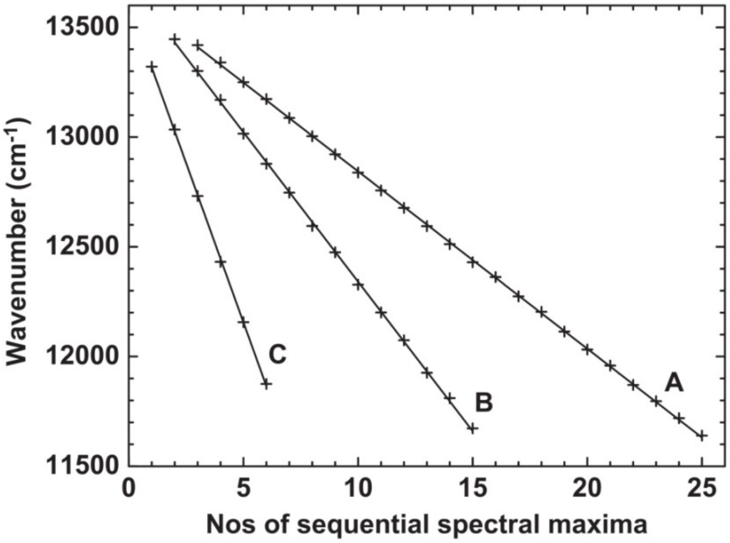

Figure 25: Three examples of linear regression fitting (solid lines) to estimated positions of sequential spectral maxima (crosses) for different fiber tail lengths l: (A) l = 769 mm, (B) l = 479 mm, (C) l = 240 mm. To estimate the spectral position of a modulation maximum, a spectral region comprising about 0.8 of an interval between the two adjacent major minima was fitted with a Gaussian curve; the standard error of Gaussian peak positions found by our nonlinear least-squares fitting software did not generally exceed 2 cm^{-1} and is depicted as the thickness of horizontal lines of the crosses. Data are obtained with a 200 nm SNOM tip.

In other cases, due to the fiber's spectral dispersion, the frequency dependence of peak positions is still smooth but not linear, which means that Δf and OPD slightly depend on the exact spectral position within the chosen spectral interval, and the same spectral position have to be chosen to compare OPD values obtained with different fiber tail lengths l.

Multimode fibers terminated by two different bent-type SNOM tips with Cr/Al coating have been studied in the two-mode regime using our MSM-based experimental technique, which allows the evaluation of OPD generated by a short metal-coated tapered tip region and of corresponding intermodal dispersion.

5.3.1. MSM studies of a 200 nm SNOM tip [IV, V]

For our sample of a 200 nm SNOM tip, spectra of the transmitted broadband light have been measured for ten different lengths l of the fiber tail. [IV] It turned out that in a certain spectral interval centered at $\lambda \approx 800$ nm a highly regular spectral modulation of substantial visibility (between 0.12 and 0.25) could be observed, which we interpreted as MSM corresponding to the nearly two-mode interference case. The modulation is less regular (becoming rather chaotic) at shorter wavelengths where an increasing number of photonic modes can pass the SNOM tip while retaining comparable amplitudes. At longer wavelengths the modulation visibility drops along with the transmitted light intensity. Thus we selected a little bit less than 2000 cm^{-1} broad spectral region around the central frequency of 12500 cm^{-1} to study the OPD for two major modes transmitted in this region. Three examples of spectral modulation observed for different l are shown in Fig. 23. Corresponding examples of the frequency dependence of spectral peak positions are shown in Fig. 25 along with the linear regression fittings (see the caption for more details). Quite good linear dependences result in uniform OPD values over the chosen spectral interval.

The OPD values τ found for ten different fiber tail lengths l are shown in Fig. 26 (see the caption for more details). The OPD value is assumed to depend linearly on l due to the presumable uniformity of the fiber inherent intermodal dispersion along the fiber length. The linear fit for the ten experimental points according to the expression

$$\tau(l) = A + Dl \tag{5.1}$$

is shown in Fig. 26 along with its extrapolation to $l = 0$.

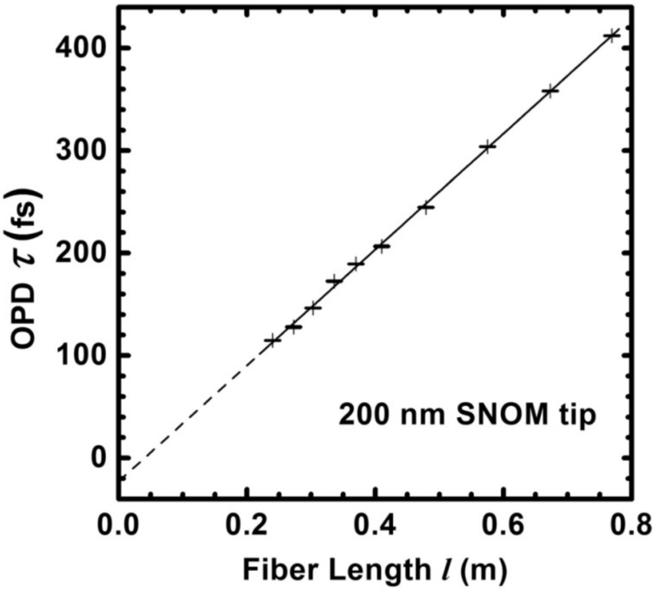

Figure 26: Linear fit (solid line) to ten experimental $\tau(l)$ points (crosses) obtained for fiber tail lengths l from 769 mm to 240 mm, extrapolated to $l = 0$ (dashed line). The thicknesses of vertical and horizontal lines forming the crosses represent respectively the precision of fiber tail length measurements (better than 2 mm) and the precision of OPD values (1.6 fs or better) derived from the tilt parameter standard error obtained by linear regression fitting of the estimated spectral maxima positions as shown in Fig. 25.

The parameter $A = \tau(0)$, for which we obtain $A = -23(3)$ fs, denotes the residual OPD value generated in the short metal-coated tapered tip of the length $l_t < 1$ mm. The parameter $D = 1/c_1 - 1/c_2$, being related to the effective phase velocities c_1 and c_2 of the two major transmitted modes, can be used as a measure of the fiber's inherent intermodal dispersion. The linear fit of our experimental data according to Eq. (5.1) results in $D = 566(6)$ fs/m. An analogous dispersion parameter can be estimated for the metal-coated tapered SNOM tip as: $D_t = A/l_t \approx -38(15)$ ps/m (this value is a low-precision estimate because the l_t value is also an estimate). The ratio of the two modal dispersion parameters can be estimated as: $D_t/D \approx -68(27)$.

The observed OPD indicates that the two major transmitted modes have different effective phase velocities in the fiber. It is reasonable to assume [63] that the lower velocity c_1 corresponds to the fundamental HE_{11} mode (LP_{01} mode according to the LP model), which has most of its energy propagating in the fiber core. According to our experimental results, in the fiber $c_2 - c_1 \approx 1.15 \cdot 10^{-4} c_1$. Our rough theoretical estimation [IV] of the mean effective phase velocity difference for two neighboring multimode fiber modes yields $\Delta c \approx 3.5 \cdot 10^{-4} c_1$. This theoretical Δc value is of the same order of magnitude with our experimental value for $c_2 - c_1$, which indicates that in our case the modes transmitted by the SNOM tip are probably retaining their character, thus supporting the assumption that our SNOM tip plays just the role of a mode filter cutting off most of the modes.

For the certain pair of photonic fiber modes, the modal dispersion parameter found for our metal-coated SNOM tip exceeds the one found for the non-coated fiber by more than an order of magnitude, but has an opposite sign. This indicates that the TM_{01} mode, which has somewhat higher phase velocity in the non-coated fiber tail region, has due to stronger interaction with plasmons a lower phase velocity in the metal-coated tip region, for which the difference of the mean phase velocities of the two (apparently TM_{01} and HE_{11}) modes can be evaluated as: $c_2 - c_1 \approx -0.0078(35)c_1$. To explain such differences of phase velocities one can assume that in our metal-coated tip the TM_{01} mode virtually transforms into a surface plasmon mode.

Due to the fact that for metals the bulk plasmon frequency ω_p lies deep in UV region, in our case the low-frequency condition $\omega \ll \omega_p$ is fulfilled, which allows us to use the formula in Eqs. (2.7) and (2.8). If assuming a very weak coupling of the fundamental HE_{11} mode to SPPs and a virtually complete conversion of the TM_{01} mode into an SPP mode, one can obtain from Eq. (2.8):

$$\frac{c_1}{c_2} - 1 \approx \alpha \frac{n_d^2 \omega^2}{2\omega_p^2} \tag{5.2}$$

Taking $\hbar\omega_p \approx 15$ eV for metallic aluminum [65, 66] and $n_d \approx 1.46$ for fused silica, for $\hbar\omega \approx 1.55$ eV (corresponding to $\lambda \approx 800$ nm) Eq. (5.2) yields: $c_2 - c_1 \approx -0.011\alpha c_1$. This value is quite well compatible with our experimental evaluation $c_2 - c_1 \approx -0.0078(35)c_1$; still the latter's low precision does not allow any reliable evaluation of the α factor. Nevertheless, our experimental results can be considered as an indicator of a mode-selective coupling of photons to surface plasmons of the SNOM tip metal coating.

5.3.2. MSM studies of a 150 nm SNOM tip [V]

Understandably, due to reduced mode-cutoff wavelengths [27], for a 150 nm SNOM tip MSM effects can be expected in a blue-shifted spectral region compared to the case of a 200 nm SNOM tip. In course of a new series of MSM experiments we performed partial scanning of the SMA 2d-position range, focusing more attention on finding "proper" adjustments of the fiber tail input in relation to the exciting light field, which enabled us to apply the two-mode model in a broader spectral region between 640 and 760 nm. It appeared to be very difficult to find any certain SMA position adjustment yielding regular spectral modulation over this entire region at once. However, it was easier to find adjustments yielding such modulation in different shorter spectral intervals within this region.

We found that at least two different types of regular modulation patterns with visibilities varying between 0.02 and 0.4 could be obtained with different SMA positions. One of them (T1) exhibits shorter-period regular modulation, which mostly does not span for long intervals, but seems to possess nearly constant period in the frequency domain regardless of the spectral location within the broader region.

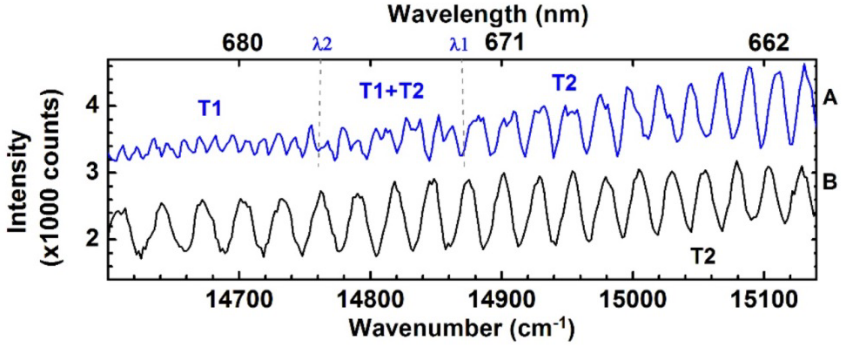

Figure 27: Two examples of spectra observed for our 150 nm SNOM tip with different fiber tail lengths: (A) $l = 1488$ mm, (B) $l = 1330$ mm. Spectrum A exhibits T2-type modulation pattern in the wavelength region $\lambda < \lambda 1 \approx 672.5$ nm and T1-type pattern in the region $\lambda > \lambda 2 \approx 677.5$ nm; a mixed (T1+T2) "chaotic" pattern can be observed in the intermediate region $\lambda 1 < \lambda < \lambda 2$. Spectrum B exhibits T2-type pattern over the entire range displayed; the corresponding modulation period increases with λ. Signal collection time 3000 s.

The second pattern type (T2), which was harder to obtain due to its high sensitivity to the SMA position (being first encountered just by chance), exhibits larger modulation period and can be observed spanning over longer spectral intervals. In spite of the modulation regularity, T2 patterns clearly exhibit smooth frequency dependence of the modulation period. Spectra containing T1 and T2 modulation patterns have been studied for nine different lengths l of the fiber tail, from 1905 mm to 612 mm. As can be seen in Fig. 27, in some cases it was even possible to observe the both pattern types in different parts of the same spectrum. In Fig. 28, two sample spectra exhibiting long-range T2 modulation for slightly different lengths l are shown. It is remarkable that in both spectra at $\lambda \approx 731$ nm the modulation period frequency dependence seems to switch its sign: in both higher and lower frequency directions the modulation period smoothly decreases. Similar behavior was observed for other lengths l, although not always a modulation pattern of comparable quality and extent could be registered.

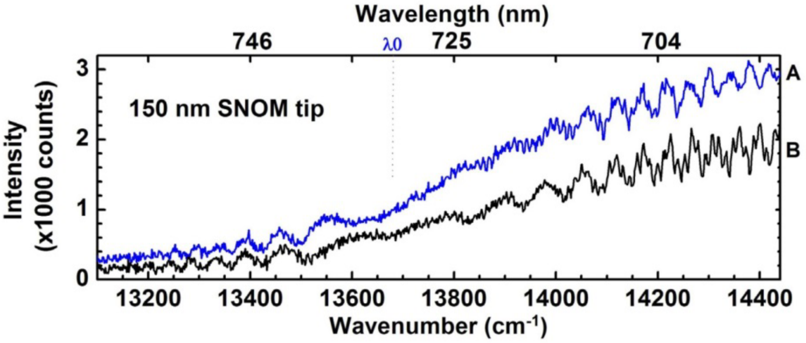

Figure 28: Two examples of spectra observed for slightly different fiber tail lengths: (A) $l = 1488$ mm, (B) $l = 1330$ mm. Both spectra exhibit T2-type modulation pattern, although a noticeable mixing can be observed with a weaker T1-type pattern having significantly shorter (nearly constant within each spectrum) modulation period. The sign of the (T2-type) modulation period λ-dependence is switched in vicinity of the special wavelength $\lambda 0 \approx 731$ nm. Signal collection time 3000 s.

It seems reasonable to assume that the two types of regular spectral modulation pattern correspond to OPD of different pairs of transmitted fiber modes. One can e.g. hypothesize that T2-type patterns correspond to OPD for TM_{01} vs. HE_{11}, while T1-type patterns – to OPD for TE_{01} vs. HE_{11} mode pairs, assuming that the fundamental HE_{11} mode should always be present. A deeper analysis of related experimental data is still to be performed, but according to our preliminary considerations the intriguing spectral behavior of T2 modulation period can be explained taking into account the spectral dispersion properties of specific multimode optical waveguide materials (fused silica with different doping for core and cladding of the fiber); the effect does not seem to be related to any specific process in a SNOM tip other than its mode-filtering ability.

Due to the scope of this work we will only discuss here issues concerning the extraction of OPD generated in the SNOM tip and its relation to photon-plasmon coupling. The earlier described method we used to analyze spectra obtained for the 200 nm SNOM tip could only be directly applied to the case of T1-type patterns featuring nearly constant modulation periods. A new technique has to be developed to analyze the frequency-dependent OPD corresponding to T2-type modulation patterns.

For nine different fiber tail lengths l, spectra containing regions of T1-tipe regular modulation have been registered at some SMA positions. These were mostly shorter regions located in different parts of the entire ~120 nm broad region examined. In such T1-intervals, positions of corresponding spectral maxima have been estimated as described in chapter 5.3.1, except that the visibility threshold was set to 0.02. As was already explained in Fig. 25 (caption), the estimated positions of sequential maxima were fitted with linear regression and corresponding OPD values found. In one case T1-type modulation could be observed in a broader spectral range; in another spectrum a broader spectral range separated two shorter T1 regions. Analysis of OPD obtained for these cases allowed us to conclude that up to our precision this parameter performs as a constant, at least in the spectral range between 640 and 740 nm. This allowed us to compare OPD values obtained for different l in different shorter spectral intervals within this range.

The OPD values τ found for different fiber tail lengths l are shown in Fig. 29 along with the linear fit according to Eq. (5.1). For the parameter $A = \tau(0)$ corresponding to OPD generated in the SNOM tip we obtain $A = -67(31)$ fs, which has the same sign as the one obtained for our 200 nm SNOM tip, but exceeds it by absolute value (though having much higher uncertainty). This difference could be a consequence of using slightly different spectral range, but involvement of a different pair of modes (e.g. TE_{01} and HE_{11}) seems even more plausible. For the fiber dispersion parameter we find: $D = 1.93(3)$ ps/m. The dispersion is more than 3 times higher than it was found in our experiments with 200 nm SNOM tip – again, this seems much better explainable by involvement of the different pair of modes. If c_1 and c_3 are the effective phase velocities of these fiber modes, we have $D = 1/c_1 - 1/c_3$. We can readily estimate the SNOM tip dispersion parameter as: $D_t = A/l_t \approx -112(67)$ ps/m; the ratio of the two modal dispersion parameters can be estimated as: $D_t/D \approx -58(35)$, which is already much closer to the value we found for our 200 nm SNOM tip.

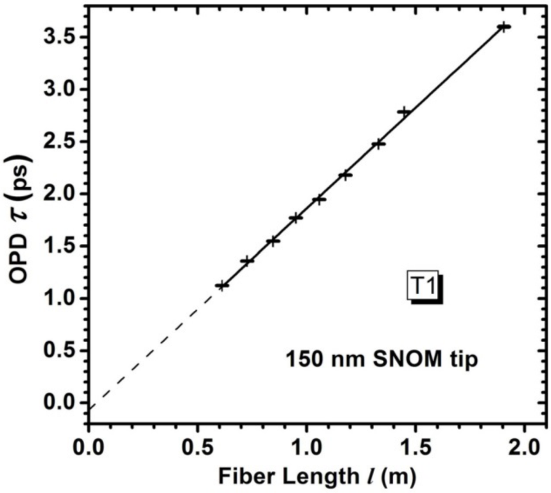

Figure 29: Linear fit (solid line) to experimental $\tau(l)$ points (crosses) obtained from T1-type modulation patterns for fiber tail lengths l from 1905 mm to 612 mm, extrapolated to $l = 0$ (dashed line). The thicknesses of vertical and horizontal lines forming the crosses represent respectively the precision of fiber tail length measurements (2 mm or better) and the precision of OPD values (18 fs or better) derived from the standard error of the tilt parameter obtained by linear regression fitting of estimated positions of spectral maxima as explained in Fig. 25.

Taking into account that for a fused silica fiber $n_d \approx 1.54$ at $\lambda \approx 700$ nm, our experimental results yield: $c_3 - c_1 \approx 3.72 \cdot 10^{-4} c_1$, which is very close to our rough theoretical estimation [IV] of the mean effective phase velocity difference for two neighboring multimode fiber modes, $\Delta c \approx 3.5 \cdot 10^{-4} c_1$. On the other hand, for the metal-coated tip region this value can be evaluated as: $c_3 - c_1 \approx -0.021(13) c_1$. In principle the situation is analogous to the one observed for (probably) different pair of modes with our 200 nm SNOM tip, as described in chapter 5.3.1. Assuming again that in the metal-coated tip one of the two modes virtually transforms into a surface plasmon mode, we can once again apply Eq. (2.8), obtaining:

$$\frac{c_1}{c_3} - 1 \approx \alpha \frac{n_d^2 \omega^2}{2\omega_p^2} \tag{5.3}$$

For the central wavelength of 700 nm ($\hbar\omega \approx 1.77$ eV) we obtain the following theoretical estimation: $c_3 - c_1 \approx -0.016 \alpha c_1$. We see that also in this case our experimental evaluation $c_3 - c_1 \approx -0.021(13) c_1$ is well compatible with the theoretical estimation, although having too high uncertainty for evaluation of the α factor in Eq. (5.3).

In conclusion to section 5.3., two independent series of experiments with two different SNOM tips with Cr/Al coating gave us quite compatible results. Multimode fibers terminated by these two SNOM tips have been studied in a two-mode regime using our proposed MSM-based experimental technique, which allows the evaluation of OPD generated in a short metal-coated tapered tip region and of corresponding intermodal dispersion. Our experimental results demonstrate that this intermodal dispersion can significantly differ from such in the multimode fiber tails and can be attributed to the mode-selective coupling of photons to surface plasmon polaritons. By absolute value, the intermodal dispersion in a SNOM tip exceeds significantly the one in a fiber tail, yet they have opposite signs. This effect can be explained by assuming that one of the two modes, which has stronger coupling to surface plasmons and thus lower phase velocity in the SNOM tip, has also higher phase velocity in an ordinary non-coated fiber. Further research is needed to determine the possible role of thin 20 nm Cr layer of the metal coating in the plasmonic effects observed.

6. MAIN ARGUMENTS PROPOSED

1. A novel nano-sized island-like diamond film with silicon vacancy (SiV) centers, which was grown by microwave plasma CVD on Si substrate, has been characterized by scanning electron microscopy, micro-Raman and photoluminescence spectroscopies. The spatial localization of SiV photoluminescent centers is found to be non-uniform, with their density in photoemitting regions exceeding one center per μm^2. Determined are the interfering factors, which hinder the registration of a single SiV center emission in thin CVD nano-diamond films.
2. Raman and photoluminescence studies of explosion-produced nanodiamond powder have revealed a significant fraction of over 30 nm sized nanocrystallites featuring nitrogen-vacancy (NV) emission. This technique can be considered for production of optical nanodiamond markers with emitting (single) NV centers.
3. The effect of a tapered metal-coated optical fiber terminated by a subwavelength aperture (a "SNOM tip") on the spectrum of the transmitted light has been investigated. Experimentally demonstrated is a mesoscopic effect of spectral modulation (MSM), which occurs due to the mode-filtering ability of a SNOM tip and to the interference of two transmitted photonic modes. The period of the regular modulation that can be observed in the output spectrum is directly related to the optical path difference (OPD) for the two modes, depending linearly on the multimode fiber length due to its inherent modal dispersion.
4. Proposed and realized has been an MSM-based experimental technique, which yields intermodal dispersion values separately for the fiber and for the SNOM tip and assumes conducting a series of spectral measurements to determine the detailed law of fiber length dependence of OPD.
5. Measurement series performed for multimode fibers terminated by two different SNOM tips with Cr/Al coating have revealed a significant modal dispersion in a SNOM tip, which is of opposite sign and of higher absolute value compared to that of the bare fiber. This effect is attributed to a mode-selective photon-plasmon coupling, offering a novel method for detection of surface plasmon polaritons generated at a metal-dielectric interface of a SNOM tip.

SUMMARY IN ESTONIAN

Eksperimentaalne nanofotoonika: üksikfootonite allikatega ja nanofiibritega seonduvad uuringud

Käesoleva töö eesmärgiks oli eksperimentaalselt panustada aktuaalsetesse üksikute kiirgustsentrite ja nanofiibritega seotud teadusuuringutesse. Selle eesmärgi teostamise nimel on autori poolt kokku pandud mitu eksperimendiseadet ja nende abil läbi viidud mitmed erinevad uuringud. Publitseeritud nanofotoonikaalaste tööde põhitulemused on järgmised:

1. Uudne, mikrolaine plasma abil CVD meetodil Si alusele kasvatatud, nanomõõdus saarekestest koosnev ja ränivakants (SiV) tsentreid sisaldav teemantkile on uuritud ja karakteriseeritud skaneeriva elektronmikroskoopia, micro-Raman ja fotoluminestsents spektroskoopia abil. On leitud et SiV kiirgustsentrite ruumiline jaotus on ebaühtlane, kusjuures tsentrite kontsentratsioon ületab kiirgavates piirkondades 1/μm^2.
2. Plahvatusliku päritolu detonatsioonilise nanoteemant-pulbri uuringud Raman- ja fotoluminestsentsspektroskoopia meetoditega aitasid tuvastada olulist fraktsiooni nanokristalliitide suurusega üle 30 nm, kust on registreeritud lämmastikvakants (NV) tsentrite kiirgust. See tehnoloogia võib sobida kiirgavate NV tsentritega optiliste nanoteemant-markerite tootmiseks.
3. Uuritud on optilise fiibri sub-lambda väljundavaga "SNOM teraviku" (külgedelt metallikihiga kaetud kooniliselt kitseneva kvartssüdamiku osa) mõju läbilastud valguse spektrile. On eksperimentaalselt demonstreeritud mesoskoopiline spektraalmodulatsiooni (MSM) efekt, mis tekib tänu SNOM otsiku võimele selekteerida optilises fiibris levivaid fotoonseid moode ja kahe läbilastud moodi interferentsile. Väljundspektris nähtava regulaarse modulatsiooni periood on otseselt seotud nende kahe moodi optiliste teepikkuste erinevusega (OTE), lineaarselt sõltudes fiibri pikkusest sellele omase mooddispersiooni tõttu.
4. Eraldi fiibris ja SNOM otsikus mooddispersiooni määramiseks on välja pakutud ja realiseeritud MSM efektil põhinev eksperimentaalmetoodika, mis eeldab spektraalmõõtmiste seeria läbiviimist leidmaks OTE detailsemat sõltuvust fiibri pikkusest.
5. Kahe erineva SNOM teravikuga fiibritel läbi viidud mõõtmisseeriad lubasid mõlemal juhul tuvastada Cr/Al metallkattega teravikus mooddispersioon, mis on vastupidise märgiga ja suurema absoluutväärtusega võrreldes katmata fiibriga. See efekt on seletatav footonite mood-selektiivse interaktsiooniga pinnaplasmonitega, pakkudes uudset metoodikat SNOM teraviku metall-dielektrik piirpinnal genereeritavate pinnaplasmon-polaritonide detekteerimiseks.

SUMMARY

Experimental nanophotonics: single-photon sources- and nanofiber-related studies

The aim of this work was to contribute experimentally to the basic research in topical fields of single emitter centers and nanofibers. For this purpose several experimental setups have been designed, built and used by the author to perform several different studies. The main published results are:

1. A novel nano-sized island-like diamond film with silicon vacancy (SiV) centers, which was grown by microwave plasma CVD on Si substrate, has been characterized by scanning electron microscopy, micro-Raman and photoluminescence spectroscopies. The spatial localization of SiV photoluminescent centers is found to be non-uniform, with their density in photoemitting regions exceeding one center per μm^2.
2. Raman and photoluminescence studies of explosion-produced detonation nanodiamond (DND) powder have revealed a significant fraction of over 30 nm sized nanocrystallites featuring well-pronounced nitrogen-vacancy (NV) emission. This technique can be considered for production of optical nanodiamond markers with emitting NV centers.
3. The effect of a tapered metal-coated optical fiber terminated by a subwavelength aperture (a “SNOM tip”) on the spectrum of the transmitted light has been investigated. Experimentally demonstrated is a mesoscopic effect of spectral modulation (MSM), which occurs due to the mode-filtering ability of a SNOM tip and to the interference of two transmitted photonic modes. The period of the regular modulation that can be observed in the output spectrum is directly related to the optical path difference (OPD) for the two modes, depending linearly on the multimode fiber length due to its inherent modal dispersion.
4. Proposed and realized has been an MSM-based experimental technique, which yields intermodal dispersion values separately for the fiber and for the SNOM tip and assumes conducting a series of spectral measurements to determine the detailed law of fiber length dependence of OPD.
5. Measurement series performed for multimode fibers terminated by two different SNOM tips with Cr/Al coating have revealed a significant modal dispersion in a SNOM tip, which is of opposite sign and of higher absolute value compared to that of the bare fiber. This effect is attributed to a mode-selective photon-plasmon coupling, offering a novel method for detection of surface plasmon polaritons generated at a metal-dielectric interface of a SNOM tip.

ACKNOWLEDGEMENTS

At first I would like to thank my supervisors. I am very grateful to Dr. Viktor Palm for teaching experimental methods and writing skills. Dr. Ilmo Sildos made good job for managing the project and holding the workgroup together. Dr. Vladimir Hizhnyakov made me understand the big picture of my field.

I am thankful for valuable discussions with Dr. Harry Alles, Dr. Aleksander Rebane and his wife.

Special thanks go to the homeless physicists refuge.

I am grateful to coworkers from the laboratory of laser spectroscopy, specially Dr. Valter Kiisk for experimental support, Dr. Raivo Jaaniso for SNOM tips. Dr. Erko Jalviste provided a lot of assistance in high-energy optical measurements.

Finally I would like to thank Kristi, parents and friends for loving and supporting me.

EXTRAS

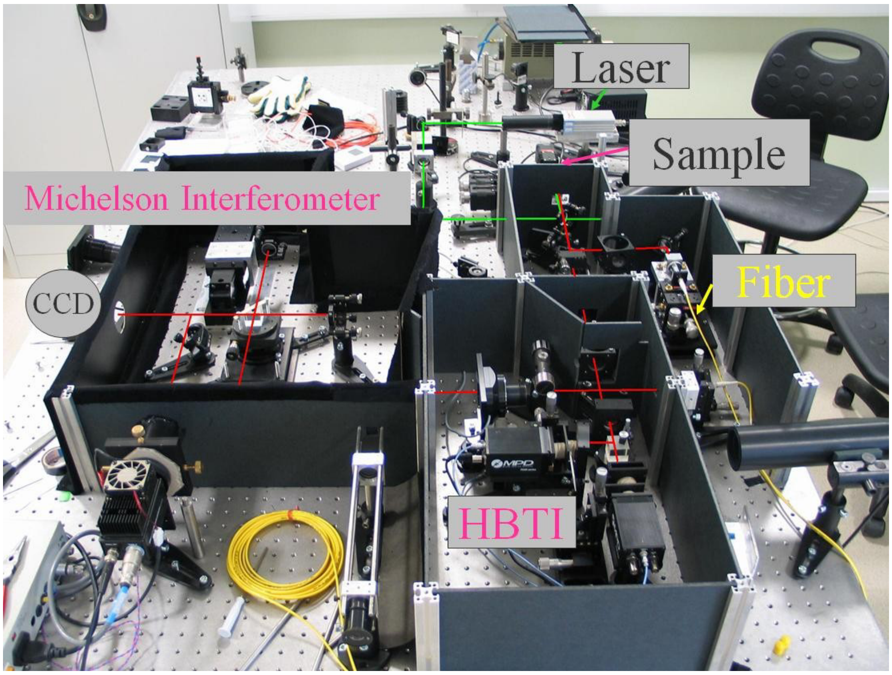

Figure 30: A photo of our vibration-stabilized optical table with an optical setup under construction [67], illustrating some practical design principles used. HBTI designates a Hanbury Brown and Twiss interferometer assembly.

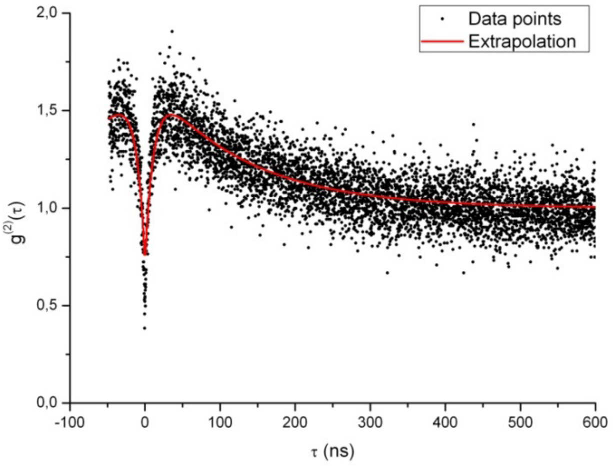

Figure 31: An example of second order correlation function obtained for a single NV defect center in diamond using a setup sketched in Fig. 8. Details available in Ref. [68].

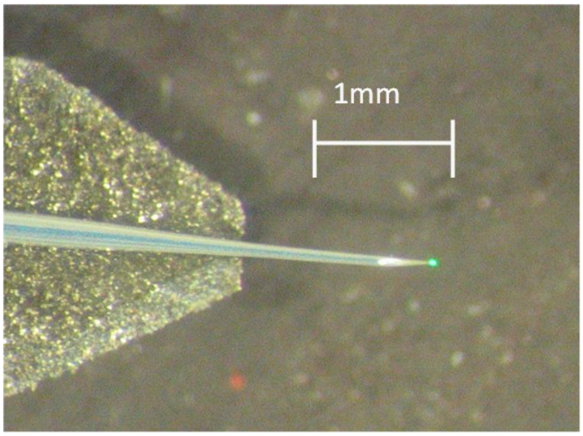

Figure 32: Microscopic image of our 200 nm bent-type SNOM tip with Cr/Al coating. The tip is bent towards the viewer; green laser light can be observed exiting the output aperture. [67]

REFERENCES

1 Basche, T., Moerner, W.E., Orrit, M., and Wild, U.P. (Eds.), “Single-Molecule Optical Detection, Imaging and Spectroscopy”, VCH, Weinheim, 1997.

2 Orrit, M., “Single-molecule spectroscopy: The road ahead”, J. Chem. Phys., 117(24), 10938–10946 (2002).

3 Kulzer, F., Xia, T., and Orrit, M., “Single Molecules as Optical Nanoprobes for Soft and Complex Matter”, Angew. Chem. Int. Ed., 49, 854–866 (2010).

4 Kulzer, F. and Orrit, M., “Single-Molecule Optics”, Ann. Rev. Phys. Chem., 55, 585–611 (2004).

5 Xie, X.S. and Trautman, K.J., “Optical Studies of Single Molecules at Room Temperature”, Ann. Rev. Phys. Chem., 49, 441–480 (1998).

6 Moerner, W.E., “Single-photon sources based on single molecules in solids”, New J. Phys., 6(88), 1–21 (2004).

7 Santori, C., Fattal, D., Vuckovic, J., Solomon, G.S., and Yamamoto, Y., “Single-photon generation with InAs quantum dots”, New J. Phys., 6(89), 1–16 (2004).

8 Aichele, T., Zwiller, V., and Benson, O., “Visible single-photon generation from semiconductor quantum dots”, New J. Phys., 6(90), 1–13 (2004).

9 Castelletto, S.A. and Scholten, R.E., “Heralded single photon sources: a route towards quantum communication technology and photon standards”, Eur. Phys. J. Appl. Phys., 41, 181–194 (2008).

10 Zaitsev, A., “Vibronic spectra of impurity-related optical centers in diamond”, Phys. Rev. B, 61(19), 12909–12922 (2000).

11 Wang, C., “A Solid-State Single Photon Source Based on Color Centers in Diamond”, PhD thesis, Ludwig-Maximilians-Universität München, Germany, 2007.

12 Kurtsiefer, C., Mayer, S., Zarda, P., and Weinfurter, H., “Stable Solid-State Source of Single Photons”, Phys. Rev. Lett., 85(2), 290–293 (2000).

13 Wang, C., Kurtsiefer, C., Weinfurter, H., and Burchard, B., “Single photon emission from SiV centres in diamond produced by ion implantation”, J. Phys. B: At. Mol. Opt. Phys., 39, 37–41 (2006).

14 Gaebel, T., Popa, I., Gruber, A., Domhan, M., Jelezko, F., and Wrachtrup, J., “Stable single-photon source in the near infrared”, New J. Phys., 6(98), 1–7 (2004).

15 Martinovich, V.A., Turukhin, A.V., Zaitsev, A.M., and Gorokhovsky, A.A., “Photoluminescence spectra of xenon implanted natural diamonds”, J. Lumin., 102–103, 785–790 (2003).

16 Verberk, R. and Orrit, M., “Photon statistics in the fluorescence of single molecules and nanocrystals: Correlation functions versus distributions of on- and off-times”, J. Chem. Phys., 119(4), 2214–2222 (2003).

17 Bernard, J., Fleury, L., Talon, H., and Orrit, M., “Photon bunching in the fluorescence from single molecules: A probe for intersystem crossing”, J. Chem. Phys., 98(2), 850–859 (1993).

18 Basche, T., Moerner, W.E., Orrit, M., and Talon, H., “Photon antibunching in the fluorescence of a single dye molecule trapped in a solid”, Phys. Rev. Lett., 69(10), 1516–1519 (1992).

19 Ambrose, W.P., Basche, T., and Moerner, W.E., “Detection and spectroscopy of single pentacene molecules in a p-terphenyl crystal by means of fluorescence excitation”, J. Chem. Phys. 95(10), 7150–7163 (1991).

20 Moerner, W.E. and Kador L., “Optical detection and spectroscopy of single molecules in a solid”, Phys. Rev. Lett., 62(21), 2535–2538 (1989).

21 Palm, V., Rebane, K.K., and Suisalu, A., “Line Width Study in Fluorescence Excitation Spectra of Single Pentacene Molecules Introduced as Impurities in p-Terphenyl Crystal”, J. Phys. Chem., 98(9), 2219–2221 (1994).

22 Rabeau, J.R., Chin, Y.L., Prawer, S., Jelezko, F., Gaebel, T., and Wrachtrup, J., “Fabrication of single nickel-nitrogen defects in diamond by chemical vapor deposition”, Appl. Phys. Lett, 86, 131926 (2005).

23 Collins, A.T., Allers, L., Wort, C.J.H., and Scarsbrook, G.A., “The annealing of radiation damage in De Beers colorless CVD diamond”, Diam. Relat. Mater., 3(4–6), 932–935 (1994).

24 Moerner, W.E., Plakhotnik, T., Irngartinger, T., Croci, M., Palm, V., and Wild, U.P., “Optical Probing of Single Molecules of Terrylene in a Shpol’skii Matrix: A Two-State Single-Molecule Switch”, J. Phys. Chem., 98(30), 7382–7389 (1994).

25 Hlubina, P., “The mutual interference of modes of a few-mode fibre waveguide analysed in the frequency domain”, J. Mod. Opt., 42(12), 2385–2399 (1995).

26 Hlubina, P., “Experimental demonstration of the spectral interference between two linearly polarized modes at the output of a fibre waveguide excited by a low-coherence source“, J. Mod. Opt., 43(8), 1745–1752 (1996).

27 Novotny, L. and Hafner, C., “Light propagation in a cylindrical waveguide with a complex, metallic, dielectric function”, Phys. Rev. E, 50(5), 4094–4106 (1994).

28 Jelezko, F. and Wrachtrup, J., “Single defect centres in diamond: A review”, phys. stat. sol. (a), 203(13), 3207–3225 (2006).

29 Davies, G. and Hamer, M.F., “Optical Studies of 1.945 eV vibronic band in diamond”, Proc. R. Soc. Lond. A, Math. Phys. Eng. Sci., 348(1653), 285–298 (1976).

30 Jelezko, F., Gaebel, T., Popa, I., Domhan, M., Gruber, A., and Wrachtrup, J., “Observation of Coherent Oscillation of a Single Nuclear Spin and Realization of a Two-Qubit Conditional Quantum Gate”, Phys. Rev. Lett., 93(13), 130501 (2004).

31 Vavilov, V.S., Gippius, A.A., Zaitsev, A.M., Deryagin, B.V., Spitsyn, B.V., and Aleksenko, A.E., "Investigation of the cathodoluminescence of epitaxial diamond films”, Sov. Phys. Semicond., 14, 1078–1079 (1980).

32 Zaitsev, A.M., Vavilov, V.S., Gippius, A.A., “Cathodoluminescence of diamond associated with silicon impurity”, Sov. Phys. Leb. Inst. Rep., 10, 15–17 (1981).

33 Clark, C.D., Kanda, H., Kiflawi, I., and Sittas, G., “Silicon defects in diamond”, Phys. Rev. B, 51(23), 16681–16688 (1995).

34 Brown, S.W. and Rand, S.C., “Site symmetry analysis of the 738 nm defect in diamond”, J. Appl. Phys., 78(6), 4069–4075 (1995).

35 Goss, J.P., Jones, R., Breuer, S.J., Briddon, P.R., and Öberg, S., “The twelve-line 1.682 eV luminescence center in diamond and the vacancy-silicon complex”, Phys. Rev. Lett., 77(14), 3041–3044 (1996).

36 Ruan, J., Choyke, W.J., and Partlow, W.D., “Si impurity in chemical vapor deposited diamond films”, Appl. Phys. Lett., 58(3), 295–297 (1991).

37 Sternschulte, H., Thonke, K., Sauer, R., Münzinger, P.C., and Michler, P., “1.681-eV luminescence center in chemical-vapor-deposited homoepitaxial diamond films”, Phys. Rev. B, 50(19), 14554–14560 (1994).

38 Ugur, A., “Silicon Vacancy Defects in Diamond as Single Photon Source”, MSc thesis, Technische Universität München, Germany, 2006.

39 Merson, T.D., Castelletto, S., Aharonovich, I., Turbic, A., Kilpatrick, T.J., and Turnley, A.M., “Nanodiamonds with silicon vacancy defects for nontoxic photostable fluorescent labeling of neural precursor cells”, Opt. Lett., 38(20), 1470–1473 (2013).

40 Maier, S.A., “Plasmonics: Fundamentals and Applications”, Springer, Berlin, 2007.

41 Ritchie, R.H., “Plasma losses by fast electrons in thin films”, Phys. Rev., 106(5), 874–881 (1957).

42 Barnes, W.L., Dereux, A., and Ebbesen, T.W., “Surface plasmon subwavelength optics”, Nature, 424(6950), 824–830 (2003).

43 Ozbay, E., “Plasmonics: emerging photonics and electronics at nanoscale dimensions”, Science, 311(5758), 189–193 (2006).

44 Raether, H., “Surface Plasmons on Smooth and Rough Surfaces and on Gratings”, Springer, Berlin, 1988.

45 Moerland, R.J., “Controlling Light Emission with Plasmonic Nanostructures”, PhD thesis, University of Twente, 2008.

46 Hanbury Brown, R. and Twiss, R.Q., “Correlation between photons in two coherent beams of light”, Nature, 177(4497), 27–32 (1956).

47 Trautman, J.K. and Macklin, J.J., “Time-resolved spectroscopy of single molecules using near-field and far-field optics”, Chem. Phys., 205(1–2), 221–229 (1996).

48 Moerner, W.E. and Fromm, D.P., “Methods of single-molecule fluorescence spectroscopy and microscopy”, Rev. Sci. Instrum., 74(8), 3597–3619 (2003).

49 Vlasov, I.I., Barnard, A.S., Ralchenko, V.G., Lebedev, O.I., Kanzyuba, M.V., Saveliev, A.V., Konov, V.I., and Goovaerts, E., “Nanodiamond photoemitters based on strong narrow-band luminescence from silicon-vacancy defects”, Adv. Mater., 21(7), 808–812 (2009).

50 Bachmann, P.K. and Wiechert, D.U., “Optical characterization of diamond”, Diam. Relat. Mater., 1(5–6), 422–433 (1992).

51 Chung, P.-H., Perevedentseva, E., Tu, J.-S., Chang, C.C., and Cheng, C.-L., “Spectroscopic study of bio-functionalized nanodiamonds”, Diam. Relat. Mater., 15(4–8), 622–625 (2006).

52 Balasubramanian, G., Chan, I.Y., Kolesov, R., Al-Hmoud, M., Tisler, J., Shin, C., Kim, C., Wojcik, A., Hemmer, P.R., Krueger, A., Hanke, T., Leitenstorfer, A., Bratschitsch, R., Jelezko, F., and Wrachtrup, J., “Nanoscale imaging magnetometry with diamond spins under ambient conditions”, Nature, 455(7213), 648–652 (2008).

53 Rabeau, J.R., Stacey, A., Rabeau, A., Prawer, S., Jelezko, F., Mirza, I., and Wrachtrup, J., “Single Nitrogen Vacancy Centers in Chemical Vapor Deposited Diamond Nanocrystals”, Nano Lett., 7(11), 3433–3437 (2007).

54 Boudou, J.-P., Curmi, P.A., Jelezko, F., Wrachtrup, J., Auber, P., Sennour, M., Balasubramanian, G., Reuter, R., Thorel, A., and Gaffet, E., “High yield fabrication of fluorescent nanodiamonds”, Nanotechnology, 20(23), 235602 (2009).

55 Schrand, A.M., Hens, S.A.C., and Shenderova, O.A., "Nanodiamond Particles: Properties and Perspectives for Bioapplications", Crit. Rev. Solid State Mater. Sci., 34(1–2), 18–74 (2009).
56 Svergun, D.I., "Determination of the regularization parameter in indirect-transform methods using perceptual criteria", J. Appl. Crystallogr., 25(4), 495–503 (1992).
57 Ager, J.W., Veirs, D.K., and Rosenblatt, G.M., "Spatially resolved Raman studies of diamond films grown by chemical vapor deposition", Phys. Rev. B, 43(8), 6491–6499 (1991).
58 Mochalin, V.N. and Gogotsi, Y., "Wet Chemistry Route to Hydrophobic Blue Fluorescent Nanodiamond" J. Am. Chem. Soc., 131(13), 4594–4595 (2009).
59 Hu, S., Tian, F., Bai, P., Cao, S., Sun, J., and Yang, J., "Synthesis and luminescence of nanodiamonds from carbon black", Mater. Sci. Eng. B, 157(1–3), 11–14 (2009).
60 Sun, Z., Shi, J.R., Tay, B.K., and Lau, S.P., "UV Raman characteristics of nanocrystalline diamond films with different grain size", Diam. Relat. Mater., 9(12), 1979–1983 (2000).
61 Hlubina, P., "Coherence of light at the output of a fibre waveguide analysed in the space-frequency domain", J. Mod. Opt., 42(7), 1407–1426 (1995).
62 Snyder, A.W. and Love, J.D., "Optical waveguide theory", Chapman and Hall, New York, 1983.
63 Okamoto, K., "Fundamentals of Optical Waveguides", Elsevier Academic Press, San Diego, 2006.
64 Marcuse, D., "Light transmission optics", Van Nostrand Reinhold Company, New York, 1972.
65 Shiles, E., Sasaki, T., Inokuti, M., and Smith, D.Y., "Self-consistency and sum-rule tests in the Kramers-Kronig analysis of optical data: Applications to aluminum", Phys. Rev. B, 22(4), 1612–1628 (1980).
66 Blaber, M.G., Arnold, M.D., and Ford, M.J., "Search for the ideal plasmonic nanoshell: the effects of surface scattering and alternatives to gold and silver", J. Phys. Chem. C, 113(8), 3041–3045 (2009).
67 Palm, V., Pärs, M., Rähn, M., Jaaniso, R., and Hizhnyakov, V., "Coherence length of photons transmitted by a subwavelength aperture", Book of Proceedings, International Commission for Optics ICO 21 – 2008 Congress: Optics for the 21st Century, Sydney, Australia, 7–10 July 2008, 123 (2008).
68 Rähn, M., "Üksikute kiirgustsentrite kasutamine ühe footoni allikana", MSc thesis, University of Tartu, 2008. (in Estonian)

PUBLICATIONS

CURRICULUM VITAE

Name: Mihkel Rähn
Date of birth: August 1, 1983, Viljandi, Estonia
Nationality: Estonian
Address: Ravila 14c, Tartu, 50411
Phone: +372 737 4742
E-mail: mihkel.rahn@ut.ee
Position: engineer, University of Tartu (UT), Institute of Physics (IP)

Education:
UT, MSc *cum laude* 2008 (fundamental physics)
UT, BSc 2006 (physics)
Viljandi C.R. Jakobson Gymnasium 2002

Language Skills:
Estonian (mother tongue)
English (speaking, writing)

Positions held:
laboratory assistant, UT IP 2007–2009
engineer, UT IP 2009–

R&D Activity:

1. Main research subjects:
   Generation of single photons with application in quantum optics experiments

2. Publications included in the thesis:
   1) Basov, A.A.; Rähn, M.; Vlasov, I.I.; Sildos, I.; Bolshakov, A.P.; Golubev, V.G.; Ralchenko, V.G. (2009). Spatial localization of Si-vacancy photoluminescent centers in a thin CVD nanodiamond film. Physica Status Solidi A – Applications and Materials Science, 206(9), 2009–2011.
   2) Vlasov, I.; Shenderova, O.; Turner, S.; Lebedev, O.; Basov, A.; Sildos, I.; Rähn, M.; Shiryaev, A.; Van Tendeloo, G. (2010). Nitrogen and luminescent nitrogen-vacancy defects in detonation nanodiamond. Small, 6(5), 687–694.
   3) Rähn, M.; Pärs, M.; Palm, V.; Jaaniso, R.; Hizhnyakov, V. (2010). Mesoscopic Effect of Spectral Modulation for the Light Transmitted by a SNOM Tip. Optics Communications, 283(11), 2457–2460.
   4) Palm, V.; Rähn, M.; Hizhnyakov, V. (2012). Modal dispersion due to photon–plasmon coupling in a SNOM tip. Optics Communications, 285, 4579–4582.
   5) Palm, V.; Rähn, M.; Jäme, J.; Hizhnyakov, V. (2012). Excitation of surface plasmons in Al-coated SNOM tips. Proc. SPIE 8457, Plasmonics: Metallic Nanostructures and Their Optical Properties X, 84572S; doi:10.1117/12.929719

3. Scholarships granted:

2009	Kristjan Jaak Scholarship for participation in International Summer School on Biophotonics
2010	Kristjan Jaak Scholarship for a laboratory visit to Montana University, USA
2010	Kristjan Jaak Scholarship for participation in an international conference
2011, 2012	FMTDK support for participation in international conferences

4. Other scientific activities:
   A Jury member of Estonian Physics Olympiad from 2006–

ELULOOKIRJELDUS

Nimi: Mihkel Rähn
Sünniaeg: 1. august 1983, Viljandi
Kodakondsus: Eesti
Töökoht, amet: Tartu Ülikool, insener
Aadress: Ravila 14c, Tartu, 50411
Telefon: +372 737 4742
E-post: mihkel.rahn@ut.ee

Haridus (lõpetatud õppeasutused, lõpetamise aastad, omandatud kraadid, kvalifikatsioonid):
Tartu Ülikool fundamentaalfüüsika magister *cum laude* 2008
Tartu Ülikool füüsika bakalaureus 2006
Viljandi C. R. Jakobsoni nimeline gümnaasium keskharidus 2002

Keelteoskus: eesti keel emakeelena, inglise keel kõnes ja kirjas

Töökogemus (teenistuskäik):
Tartu Ülikool füüsika instituut laborant 2007–2009, insener 2009–

Teaduslik ja arendustegevus:

1. Peamised uurimisvaldkonnad: Üksikfootonite tekitamine ja rakendamine kvantoptilistes eksperimentides

2. Teesidega hõlmatud publikatsioonide loetelu
    1. Basov, A.A.; Rähn, M.; Vlasov, I.I.; Sildos, I.; Bolshakov, A.P.; Golubev, V.G.; Ralchenko, V.G. (2009). Spatial localization of Si-vacancy photoluminescent centers in a thin CVD nanodiamond film. Physica Status Solidi A – Applications and Materials Science, 206(9), 2009–2011.
    2. Vlasov, I.; Shenderova, O.; Turner, S.; Lebedev, O.; Basov, A.; Sildos, I.; Rähn, M.; Shiryaev, A.; Van Tendeloo, G. (2010). Nitrogen and luminescent nitrogen-vacancy defects in detonation nanodiamond. Small, 6(5), 687–694.
    3. Rähn, M.; Pärs, M.; Palm, V.; Jaaniso, R.; Hizhnyakov, V. (2010). Mesoscopic Effect of Spectral Modulation for the Light Transmitted by a SNOM Tip. Optics Communications, 283(11), 2457–2460.
    4. Palm, V.; Rähn, M.; Hizhnyakov, V. (2012). Modal dispersion due to photon–plasmon coupling in a SNOM tip. Optics Communications, 285, 4579–4582.
    5. Palm, V.; Rähn, M.; Jäme, J.; Hizhnyakov, V. (2012). Excitation of surface plasmons in Al-coated SNOM tips. Proc. SPIE 8457, Plasmonics: Metallic Nanostructures and Their Optical Properties X, 84572S (2012); doi:10.1117/12.929719

3. Saadud uurimistoetused ja stipendiumid

2009	Kristjan Jaagu stipendium rahvusvahelise biofotoonika suvekoolist osavõtuks
2010	Kristjan Jaagu stipendium laborikülastuseks Montana Osariigi Ülikoolis, Ameerika Ühendriikides.
2010	Kristjan Jaagu stipendium konverentsi külastuseks
2011, 2012	FMTDK toetus konverentsist osavõtuks

4. Muu teaduslik organisatsiooniline ja erialane tegevus (konverentside ettekanded, osalemine erialastes seltsides, seadusloome jms.)
   Olen Eesti Füüsikaolümpiaadi žürii liige 2006–

DISSERTATIONES PHYSICAE UNIVERSITATIS TARTUENSIS

1. **Andrus Ausmees.** XUV-induced electron emission and electron-phonon interaction in alkali halides. Tartu, 1991.
2. **Heiki Sõnajalg.** Shaping and recalling of light pulses by optical elements based on spectral hole burning. Tartu, 1991.
3. **Sergei Savihhin.** Ultrafast dynamics of F-centers and bound excitons from picosecond spectroscopy data. Tartu, 1991.
4. **Ergo Nõmmiste.** Leelishalogeniidide röntgenelektronemissioon kiiritamisel footonitega energiaga 70–140 eV. Tartu, 1991.
5. **Margus Rätsep.** Spectral gratings and their relaxation in some low-temperature impurity-doped glasses and crystals. Tartu, 1991.
6. **Tõnu Pullerits.** Primary energy transfer in photosynthesis. Model calculations. Tartu, 1991.
7. **Olev Saks.** Attoampri diapasoonis voolude mõõtmise füüsikalised alused. Tartu, 1991.
8. **Andres Virro.** AlGaAsSb/GaSb heterostructure injection lasers. Tartu, 1991.
9. **Hans Korge.** Investigation of negative point discharge in pure nitrogen at atmospheric pressure. Tartu, 1992.
10. **Jüri Maksimov.** Nonlinear generation of laser VUV radiation for high-resolution spectroscopy. Tartu, 1992.
11. **Mark Aizengendler.** Photostimulated transformation of aggregate defects and spectral hole burning in a neutron-irradiated sapphire. Tartu, 1992.
12. **Hele Siimon.** Atomic layer molecular beam epitaxy of A^2B^6 compounds described on the basis of kinetic equations model. Tartu, 1992.
13. **Tõnu Reinot.** The kinetics of polariton luminescence, energy transfer and relaxation in anthracene. Tartu, 1992.
14. **Toomas Rõõm.** Paramagnetic H^{2-} and F^+ centers in CaO crystals: spectra, relaxation and recombination luminescence. Tallinn, 1993.
15. **Erko Jalviste.** Laser spectroscopy of some jet-cooled organic molecules. Tartu, 1993.
16. **Alvo Aabloo.** Studies of crystalline celluloses using potential energy calculations. Tartu, 1994.
17. **Peeter Paris.** Initiation of corona pulses. Tartu, 1994.
18. **Павел Рубин.** Локальные дефектные состояния в CuO_2 плоскостях высокотемпературных сверхпроводников. Тарту, 1994.
19. **Olavi Ollikainen.** Applications of persistent spectral hole burning in ultrafast optical neural networks, time-resolved spectroscopy and holographic interferometry. Tartu, 1996.
20. **Ülo Mets.** Methodological aspects of fluorescence correlation spectroscopy. Tartu, 1996.
21. **Mikhail Danilkin.** Interaction of intrinsic and impurity defects in CaS:Eu luminophors. Tartu, 1997.

22. **Ирина Кудрявцева.** Создание и стабилизация дефектов в кристаллах KBr, KCl, RbCl при облучении ВУФ-радиацией. Тарту, 1997.
23. **Andres Osvet.** Photochromic properties of radiation-induced defects in diamond. Tartu, 1998.
24. **Jüri Örd.** Classical and quantum aspects of geodesic multiplication. Tartu, 1998.
25. **Priit Sarv.** High resolution solid-state NMR studies of zeolites. Tartu, 1998.
26. **Сергей Долгов.** Электронные возбуждения и дефектообразование в некоторых оксидах металлов. Тарту, 1998.
27. **Kaupo Kukli.** Atomic layer deposition of artificially structured dielectric materials. Tartu, 1999.
28. **Ivo Heinmaa.** Nuclear resonance studies of local structure in $RBa_2Cu_3O_{6+x}$ compounds. Tartu, 1999.
29. **Aleksander Shelkan.** Hole states in CuO_2 planes of high temperature superconducting materials. Tartu, 1999.
30. **Dmitri Nevedrov.** Nonlinear effects in quantum lattices. Tartu, 1999.
31. **Rein Ruus.** Collapse of 3d (4f) orbitals in 2p (3d) excited configurations and its effect on the x-ray and electron spectra. Tartu, 1999.
32. **Valter Zazubovich.** Local relaxation in incommensurate and glassy solids studied by Spectral Hole Burning. Tartu, 1999.
33. **Indrek Reimand.** Picosecond dynamics of optical excitations in GaAs and other excitonic systems. Tartu, 2000.
34. **Vladimir Babin.** Spectroscopy of exciton states in some halide macro- and nanocrystals. Tartu, 2001.
35. **Toomas Plank.** Positive corona at combined DC and AC voltage. Tartu, 2001.
36. **Kristjan Leiger.** Pressure-induced effects in inhomogeneous spectra of doped solids. Tartu, 2002.
37. **Helle Kaasik.** Nonperturbative theory of multiphonon vibrational relaxation and nonradiative transitions. Tartu, 2002.
38. **Tõnu Laas.** Propagation of waves in curved spacetimes. Tartu, 2002.
39. **Rünno Lõhmus.** Application of novel hybrid methods in SPM studies of nanostructural materials. Tartu, 2002.
40. **Kaido Reivelt.** Optical implementation of propagation-invariant pulsed free-space wave fields. Tartu, 2003.
41. **Heiki Kasemägi.** The effect of nanoparticle additives on lithium-ion mobility in a polymer electrolyte. Tartu, 2003.
42. **Villu Repän.** Low current mode of negative corona. Tartu, 2004.
43. **Алексей Котлов.** Оксианионные диэлектрические кристаллы: зонная структура и электронные возбуждения. Tartu, 2004.
44. **Jaak Talts.** Continuous non-invasive blood pressure measurement: comparative and methodological studies of the differential servo-oscillometric method. Tartu, 2004.
45. **Margus Saal.** Studies of pre-big bang and braneworld cosmology. Tartu, 2004.

46. **Eduard Gerškevitš.** Dose to bone marrow and leukaemia risk in external beam radiotherapy of prostate cancer. Tartu, 2005.
47. **Sergey Shchemelyov.** Sum-frequency generation and multiphoton ionization in xenon under excitation by conical laser beams. Tartu, 2006.
48. **Valter Kiisk.** Optical investigation of metal-oxide thin films. Tartu, 2006.
49. **Jaan Aarik.** Atomic layer deposition of titanium, zirconium and hafnium dioxides: growth mechanisms and properties of thin films. Tartu, 2007.
50. **Astrid Rekker.** Colored-noise-controlled anomalous transport and phase transitions in complex systems. Tartu, 2007.
51. **Andres Punning.** Electromechanical characterization of ionic polymer-metal composite sensing actuators. Tartu, 2007.
52. **Indrek Jõgi.** Conduction mechanisms in thin atomic layer deposited films containing TiO_2. Tartu, 2007.
53. **Aleksei Krasnikov.** Luminescence and defects creation processes in lead tungstate crystals. Tartu, 2007.
54. **Küllike Rägo.** Superconducting properties of MgB_2 in a scenario with intra- and interband pairing channels. Tartu, 2008.
55. **Els Heinsalu.** Normal and anomalously slow diffusion under external fields. Tartu, 2008.
56. **Kuno Kooser.** Soft x-ray induced radiative and nonradiative core-hole decay processes in thin films and solids. Tartu, 2008.
57. **Vadim Boltrushko.** Theory of vibronic transitions with strong nonlinear vibronic interaction in solids. Tartu, 2008.
58. **Andi Hektor.** Neutrino Physics beyond the Standard Model. Tartu, 2008.
59. **Raavo Josepson.** Photoinduced field-assisted electron emission into gases. Tartu, 2008.
60. **Martti Pärs.** Study of spontaneous and photoinduced processes in molecular solids using high-resolution optical spectroscopy. Tartu, 2008.
61. **Kristjan Kannike.** Implications of neutrino masses. Tartu, 2008.
62. **Vigen Issahhanjan.** Hole and interstitial centres in radiation-resistant MgO single crystals. Tartu, 2008.
63. **Veera Krasnenko.** Computational modeling of fluorescent proteins. Tartu, 2008.
64. **Mait Müntel.** Detection of doubly charged higgs boson in the CMS detector. Tartu, 2008.
65. **Kalle Kepler.** Optimisation of patient doses and image quality in diagnostic radiology. Tartu, 2009.
66. **Jüri Raud.** Study of negative glow and positive column regions of capillary HF discharge. Tartu, 2009.
67. **Sven Lange.** Spectroscopic and phase-stabilisation properties of pure and rare-earth ions activated ZrO_2 and HfO_2. Tartu, 2010.
68. **Aarne Kasikov.** Optical characterization of inhomogeneous thin films. Tartu, 2010.

69. **Heli Valtna-Lukner.** Superluminally propagating localized optical pulses. Tartu, 2010.
70. **Artjom Vargunin.** Stochastic and deterministic features of ordering in the systems with a phase transition. Tartu, 2010.
71. **Hannes Liivat.** Probing new physics in e+e− annihilations into heavy particles via spin orientation effects. Tartu, 2010.
72. **Tanel Mullari.** On the second order relativistic deviation equation and its applications. Tartu, 2010.
73. **Aleksandr Lissovski.** Pulsed high-pressure discharge in argon: spectroscopic diagnostics, modeling and development. Tartu, 2010.
74. **Aile Tamm.** Atomic layer deposition of high-permittivity insulators from cyclopentadienyl-based precursors. Tartu, 2010.
75. **Janek Uin.** Electrical separation for generating standard aerosols in a wide particle size range. Tartu, 2011.
76. **Svetlana Ganina.** Hajusandmetega ülesanded kui üks võimalus füüsikaõppe efektiivsuse tõstmiseks. Tartu, 2011
77. **Joel Kuusk.** Measurement of top-of-canopy spectral reflectance of forests for developing vegetation radiative transfer models. Tartu, 2011.
78. **Raul Rammula**. Atomic layer deposition of HfO_2 – nucleation, growth and structure development of thin films. Tartu, 2011.
79. **Сергей Наконечный.** Исследование электронно-дырочных и интерстициал-вакансионных процессов в монокристаллах MgO и LiF методами термоактивационной спектроскопии. Тарту, 2011.
80. **Niina Voropajeva.** Elementary excitations near the boundary of a strongly correlated crystal. Tartu, 2011.
81. **Martin Timusk.** Development and characterization of hybrid electro-optical materials. Tartu, 2012, 106 p.
82. **Merle Lust.** Assessment of dose components to Estonian population. Tartu, 2012, 84 p.
83. **Karl Kruusamäe.** Deformation-dependent electrode impedance of ionic electromechanically active polymers. Tartu, 2012, 128 p.
84. **Liis Rebane.** Measurement of the $W \to \tau\nu$ cross section and a search for a doubly charged Higgs boson decaying to τ-leptons with the CMS detector. Tartu, 2012, 156 p.
85. **Jevgeni Šablonin.** Processes of structural defect creation in pure and doped MgO and NaCl single crystals under condition of low or super high density of electronic excitations. Tartu, 2013, 145 p.
86. **Riho Vendt**. Combined method for establishment and dissemination of the international temperature scale. Tartu, 2013, 108 p.
87. **Peeter Piksarv.** Spatiotemporal characterization of diffractive and non-diffractive light pulses. Tartu, 2013, 156 p.
88. **Anna Šugai.** Creation of structural defects under superhigh-dense irradiation of wide-gap metal oxides. Tartu, 2013, 108 p.

89. **Ivar Kuusik.** Soft X-ray spectroscopy of insulators. Tartu, 2013, 113 p.
90. **Viktor Vabson**. Measurement uncertainty in Estonian Standard Laboratory for Mass. Tartu, 2013, 134 p.
91. **Kaupo Voormansik.** X-band synthetic aperture radar applications for environmental monitoring. Tartu, 2014, 117 p.
92. **Deivid Pugal.** hp-FEM model of IPMC deformation. Tartu, 2014, 143 p.
93. **Siim Pikker.** Modification in the emission and spectral shape of photostable fluorophores by nanometallic structures. Tartu, 2014, 98 p.
94. **Mihkel Pajusalu**. Localized Photosynthetic Excitons. Tartu, 2014, 183 p.
95. **Taavi Vaikjärv.** Consideration of non-adiabaticity of the Pseudo-Jahn-Teller effect: contribution of phonons. Tartu, 2014, 129 p.
96. **Martin Vilbaste.** Uncertainty sources and analysis methods in realizing SI units of air humidity in Estonia. Tartu, 2014, 111 p.